2015-02-01

Characterization of Geometrically Necessary Dislocation Content with EBSD-Based Continuum Dislocation Microscopy

Tim Ruggles
Brigham Young University - Provo

Characterization of Geometrically Necessary Dislocation Content with EBSD-Based Continuum Dislocation Microscopy

Timothy J. Ruggles

A dissertation submitted to the faculty of
Brigham Young University
in partial fulfillment of the requirements for the degree of

Doctor of Philosophy

David T. Fullwood, Chair
Eric R. Homer
Tracy W. Nelson
Michael M. Miles
Anton E. Bowden

Department of Mechanical Engineering

Brigham Young University

February 2015

ABSTRACT

Characterization of Geometrically Necessary Dislocation Content
with EBSD-Based Continuum Dislocation Microscopy

Timothy J. Ruggles
Department of Mechanical Engineering, BYU
Doctor of Philosophy

Modeling of plasticity is often hampered by the difficulty in accurately characterizing dislocation density on the microscale for real samples. It is particularly difficult to resolve measured dislocation content onto individual dislocation systems at the length scales most commonly of interest in plasticity studies. Traditionally, dislocation content is analyzed at the continuum level using the Nye tensor and the fundamental relation of continuum dislocation theory to interpret information measured by diffraction techniques, typically EBSD or High Resolution EBSD. In this work the established Nye-Kroner method for resolving measured geometrically necessary dislocation content onto individual slip systems is assessed and extended. Two new methods are also presented to relieve the ambiguity of the Nye-Kroner method. One of these methods uses modified classical dislocation equations to bypass the Nye-Kroner relation, and the other estimates the bulk dislocation density via the entry-wise one-norm of the Nye tensor. These methods are validated via a novel simulation of distortion fields around continuum fields of dislocation density based on classical lattice mechanics and then applied to actual HR-EBSD scans of a micro-indented single crystals of nickel and tantalum. Finally, a detailed analysis of the effect of the spacing between points in an EBSD scan (which is related to the step size of the numerical derivatives used in EBSD dislocation microscopy) on geometrically necessary dislocation measurements is conducted.

Keywords: EBSD, dislocation microscopy, cross-correlation, HREBSD

ACKNOWLEDGMENTS

This work presented here is the result of collaboration with a number of extraordinary researchers. I would especially like to acknowledge the assistance of my committee, Travis Rampton, Thomas Hardin, Ali Khosravani, Jay Basinger, Stuart Wright, and Brent Adams for a wealth of valuable discussion, libraries of useful code, and exceptional microscopy data.

The author also acknowledges financial support from National Science Foundation grant CMMI 1404771 and Department of Energy grant DE-SC0012587 as well as additional funding from EDAX.

TABLE OF CONTENTS

LIST OF TABLES . . . . . **vi**

LIST OF FIGURES . . . . . **vii**

NOMENCLATURE viii

Chapter 1 Introduction **1**
1.1 Background - Fundamental Continuum Dislocation Relationships 3
1.2 Background - EBSD and HREBSD 5
1.3 Background - Continuum Dislocation Microscopy 9
1.4 Scope of this work 10

Chapter 2 An improved estimate of bulk dislocation density **13**
2.1 Estimates of the entry-wise one-norm of the Nye tensor 14
2.2 Dislocation density field simulations based on classical lattice mechanics 16
2.3 Accuracy of the GND quantification using a typical minimization scheme 18
2.4 Norms of the Nye tensor for estimating GND density 19
2.5 Estimating GND density from an incomplete Nye tensor 21
2.6 Orientation sensitivity 25
2.7 Performance on a real scan 26
2.8 Conclusions 28

Chapter 3 Robust application of the Nye-Kroner equations to resolve dislocation content onto individual slip systems **31**
3.1 Optimization methods 32
3.2 Validation via simulation 33
3.3 Demonstration in deformed single crystal nickel 36
3.4 Conclusions 39

Chapter 4 A novel approach to resolving dislocation density onto individual dislocation systems based on classical dislocation mechanics **43**
4.1 The distortion matching method 44
4.2 Validation of the distortion matching method via simulation 45
4.3 Conclusions 50

Chapter 5 The effect of length scale on the measurement of geometrically necessary dislocations via EBSD continuum dislocation microscopy **53**
5.1 Methods and materials 55
5.2 Results 56
5.3 Modeling the GND density-step size relationship statistically 60
5.4 Conclusions 66

Chapter 6 Contributions and discussion 69

REFERENCES 73

LIST OF TABLES

2.1 Bulk dislocation density simulation results 29
2.2 Signal to noise of bulk dislocation density estimates 29

3.1 Effective slip systems for indented nickel 37

LIST OF FIGURES

1.1 F definitions 4
1.2 Diagram of EBSD microscope set-up 6
1.3 Hough transform 6
1.4 ROI for HREBSD 7
1.5 Illustration of the geometric calculations required for HREBSD 8

2.1 Norm performance 20
2.2 Orientation sensitivity 26
2.3 Bulk dislocation density estimates of wedge indented Ta 30

3.1 Simulated performance of the Nye-Kroner method 35
3.2 Measured dislocation density on equivalent slip system 1 38
3.3 Measured dislocation density on equivalent slip system 2 39
3.4 Measured dislocation density on equivalent slip system 3 40

4.1 Simulated performance of the distortion matching method 48
4.2 Simulated performance of the distortion matching method (multiple dislocation systems) 50

5.1 GND density map for a small scan of indented Ta 56
5.2 GND versus step size curve for wedge-indented Ta 57
5.3 GND versus step size curve for annealed materials at low step size 58
5.4 GND versus step size curve for deformed iron 59
5.5 Kacher's simulation of GND density versus step size 61
5.6 Comparison of the Skellam and Gaussian models of GND density versus step size . 63
5.7 Comparison of the Gaussian model of GND density versus step size with and without limits applied 66
5.8 Gaussian model fit to the indented Ta data 67

NOMENCLATURE

GND	Geometrically necessary dislocation
SSD	Statistically stored dislocation
α	The Nye tensor, used to express net Burgers vector in three dimensions
β	Lattice distortion tensor, the combination of the finite strain and rotation tensors
β^e	Elastic component of lattice distortion
β^p	Plastic component of lattice distortion
ε	Finite strain
ω	Finite lattice rotation tensor
ρ	Bulk, or total dislocation density (sum of the density on all slip systems)
ρ^t	Dislocation density on the t-th dislocation system
$\mathbf{b}$	Burgers vector
b	Magnitude of the Burgers vector
$\mathbf{v}$	Dislocation line vector
$\mathbf{F}$	Deformation tensor
$\mathbf{u}$	Displacement due to deformation
ν	Poisson's ratio
w^t	Weighting function for minimization
L	Raster spacing of an EBSD scan and the numerical derivative step size for lattice distortion derivatives
CRSS	Critically resolved shear stress to initiate slip for a given dislocation
SEM	Scanning electron microscope
TEM	Transmission electron microscope
μXRD	Micro X-Ray diffraction

CHAPTER 1. INTRODUCTION

Materials science is chiefly concerned with processing-properties relationships. An understanding of the micro- and mesostructure of a material (as well as its evolution in response to deformation) is essential to understanding these relationships. Understanding of processing-structure-property linkages is most often limited by the inability to characterize the structure of the material at the appropriate scale. Plasticity models have fairly successfully replicated stress strain curves for several decades, but they still do not accurately predict texture evolution at the individual crystal level, nor do they provide fundamental structure property relations such as those for ductility and strength. Not only are the hardening mechanisms not correctly captured (i.e. dislocation interactions), but the assumed stress / slip relations are inaccurate. Many of these open questions relate to phenomena of dislocation activity at the mesoscale, and there is a fundamental need to characterize and accurately model dislocation evolution at this scale.

Dislocations, their motion, nucleation, and interaction, are the key physical phenomenon behind crystal plasticity. Partially as a result of the difficulty of accurately characterizing dislocation density, most plasticity models do not address the phenomenon directly; i.e. dislocation activity and content is not typically explicitly quantified. These models, while much simpler, lack the accuracy required for analyzing and optimizing modern metals and ceramics

The drive for greater performance from engineering materials has led to the incorporation of more and more dislocation information into plasticity modeling. Currently, however, there is a dearth of real data on dislocation content that hinders the development of plasticity modeling. The objective of this work is to dramatically improve the dislocation information available at the micro- and mesoscale.

Dislocations are typically detected by observing the effect of their localized lattice distortion fields via diffraction. For several decades dislocations were characterized and quantified as discrete phenomena via transmission electron microscopy (TEM) [1, 2]. While TEM techniques

can detect distortion fields at length scales short enough to resolve individual dislocations, the leap from these localized measurements to the effect on macro, or even meso, response and related properties is difficult due to the large number of dislocations involved. Combined with the fact that sample preparation for TEM is both highly time consuming and destructive to the sample, denuding the sample of dislocations, a fully representative study of dislocations in bulk materials via TEM is problematic.

These difficulties have lead to efforts to understand dislocations at larger scales (typically at a scale where they can be modeled as continuous fields rather than discreet phenomena). Although it is difficult to measure the effects of single dislocations, the net geometric effects of a network of dislocations, treated as a continuum, are easier to deal with. Dislocations that accommodate long range distortion gradients in material associated with heterogeneous deformation are called geometrically necessary dislocations (GNDs) [3]. The net geometric effect of GNDs is typically characterized by a net Burgers vector. The definition of GNDs actually depends on the size of the implicit Burgers circuit. Statistically stored dislocations (SSDs), in contrast, accommodate homogeneous deformations and at larger length scales should not be detectable based on the distortion of the lattice because any net geometric effect they would have is counteracted by nearby dislocations of opposite sign within the Burgers circuit. Thus, the distinction between SSDs and GNDs (i.e. what dislocations are measurable via diffraction) is length scale dependent. As the length scale increases, more dislocations cancel one another, meaning that GNDs will transition to SSDs with increasing step size.

The continuum mechanics of geometrically necessary dislocation fields were well established in the 1950 [4, 5]. Recent advances in the technology to measure the geometric effects of continuum dislocation fields at lengths scales relevant to plasticity models (i.e. at subgrain levels) have allowed for dislocation information to be recovered at the meso-scale.

Continuum dislocation microscopy (CDM) depends on the recovery of local lattice distortion gradients, which may then be related to the geometrically necessary dislocation content. With the advent of micro x-ray diffraction (μXRD) (e.g. [6]) and automated electron backscatter diffraction (EBSD) [7–9] microscopy, information about the lattice orientation could be gleaned at relevant length scales. The advent of High Resolution EBSD (HREBSD) subsequently improved the resolution of this technique dramatically [10–12]. Using continuum dislocation mechanics de-

veloped by Nye and Kroner, this lattice information could be related to the dislocation content of the material (Adams, 1997). These techniques were developed into the first continuum dislocation microscopy technology [13–17]. This enables the EBSD results to be applied directly to meso-scale calculations that incorporate GND evolution and effects [18]. This paper will examine EBSD CDM, a technique favored because of its ease of implementation and superior spatial resolution as compared to μXRD [19, 20].

Although EBSD CDM is a valuable characterization technique, there are still a number of significant barriers to their wide adoption, which include the underconstrained nature of the fundamental CDM equations and the GND to SSD transition. This paper presents three novel methods of addressing the unconstrained problem: an improved version of existing Nye-Kroner methods that uses non-traditional optimization techniques, a method of estimating the bulk GND density without solving the Nye-Kroner equations, and finally a completely new method that directly relates measured lattice distortion information to the dislocation content of the material using classical dislocation mechanics. These methods are subsequently validated using a new dislocation simulation and real samples. The variability of results when different scan step sizes are used due to the GND to SSD transition is also addressed.

1.1 Background - Fundamental Continuum Dislocation Relationships

Dislocations cause distortions in the surrounding lattice. This residual elastic lattice distortion can be measured via diffraction techniques like EBSD and subsequently be used to recover the dislocation content of the material. This relationship may be determined by assuming the compatibility of the elastic and plastic deformation, i.e. that no voids have opened due to the deformation.

We define the deformation gradient as

$$\mathbf{F} = \frac{\partial \mathbf{x}}{\partial \mathbf{X}} = \frac{\partial \mathbf{u}}{\partial \mathbf{X}} + 1 \tag{1.1}$$

where $\mathbf{X}$ is the position of a given point in the undeformed material, $\mathbf{x}$ is the position of that point after deformation and $\mathbf{u}$ is the displacement of that point. This is illustrated in Figure 1.1. If we

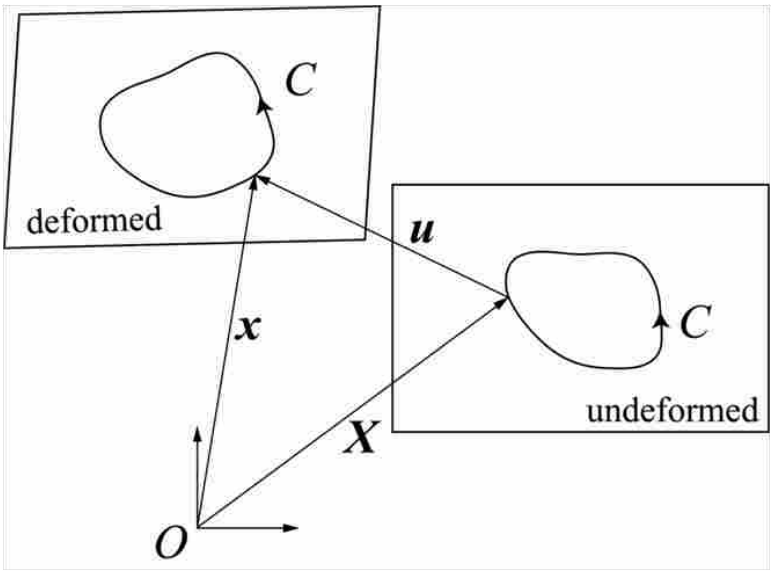

Figure 1.1: An illustration to help understand the compatibility of deformation.

assume an infinitesimal deformation, i.e.

$$|\frac{\partial \mathbf{u}}{\partial \mathbf{X}}| << 1 \tag{1.2}$$

the compatibility requires that

$$\oint_C d\mathbf{u} = \oint_C \left(\frac{\partial \mathbf{u}}{\partial \mathbf{X}}\right) \cdot d\mathbf{X} = \oint_C \left(\frac{\partial \mathbf{u}}{\partial \mathbf{X}}\right) \cdot \mathbf{s} ds = 0 \tag{1.3}$$

with $\mathbf{s}ds = d\mathbf{X}$, where C is an arbitrary circuit and $\mathbf{s}$ is a unit vector along C.

We define $\frac{\partial \mathbf{u}}{\partial \mathbf{X}}$ as the lattice distortion, β, and separate it into its plastic and elastic component as follows:

$$\frac{\partial \mathbf{u}}{\partial \mathbf{X}} = \beta = \beta^p + \beta^e \tag{1.4}$$

Combining this equation into Equation 1.3 yields:

$$\oint_C \beta^e \cdot \mathbf{s} ds = -\oint_C \beta^p \cdot \mathbf{s} ds = \mathbf{B} \tag{1.5}$$

where $\mathbf{B}$ is the plastic "closure failure" due to dislocation content, also known as the net Burgers vector (if only one dislocation passes through the circuit, it is simply the Burgers vector). Applying

Stoke's theorem, this equation becomes:

$$\iint_A \nabla \times \beta^e \cdot \mathbf{n} da = -\iint_A \nabla \times \beta^p \cdot \mathbf{n} da \tag{1.6}$$

where A is the area encompassed by the circuit C and $\mathbf{n}$ is its normal. Because this is true for an arbitrary A, we may state that:

$$\nabla \times \beta^e = -\nabla \times \beta^p = \alpha \tag{1.7}$$

where α is a second order tensor that operates on a plane normal to produce the net Burgers vector for a circuit on that plane. We refer to this tensor as the Nye tensor and Equation 1.7 as the fundamental relation of dislocation theory [4, 5]. Finally, the Nye tensor may be related to the dislocation content of individual slip systems as follows,

$$\alpha = \sum_{t=1}^{N} \rho^t \mathbf{b}^t \otimes \mathbf{v}^t \tag{1.8}$$

where ρ^t, $\mathbf{b}^t$, and $\mathbf{v}^t$ are the dislocation density, Burgers vector, and line vector of each "dislocation system," where a dislocation system is defined here as a unique combination of Burgers vector and line vector for a pure edge or screw dislocation. Dislocations of mixed character are assumed to be represented as linear combinations of other dislocation systems.

1.2 Background - EBSD and HREBSD

Continuum dislocation microscopy first requires local measurement of lattice geometry, in this case, via EBSD. EBSD patterns are collected in a scanning electron microscope (SEM). As the electron beam is held in one spot, high energy, back-scattered electrons diffract on their way back out of the sample. The resulting back scattered diffraction pattern is collected using a CCD (charge coupled device) camera and stored electronically. This process is illustrated in Figure 1.2

Although phenomenon of EBSD was known and understood for over fifty years [22], it was not until the early 1990s that researchers developed automated indexing of EBSD patterns [7–9]. These techniques employ the Hough transform as a computer vision technique to accurately index (determine the orientation of) these patterns. A number of alternate indexing methods have also

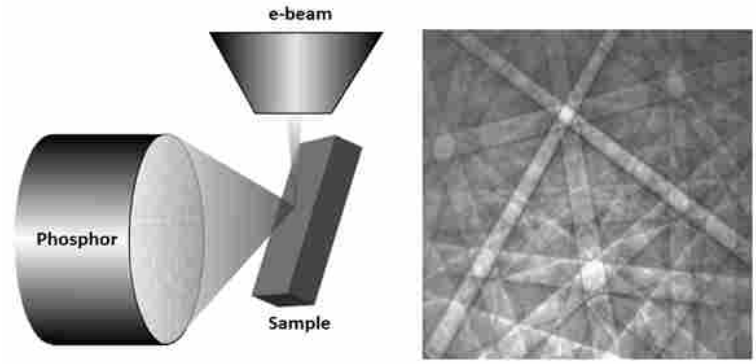

Figure 1.2: Schematic of EBSD microscope set-up (left) and an example of an EBSD pattern from a silicon sample (right). Image courtesy of [21].

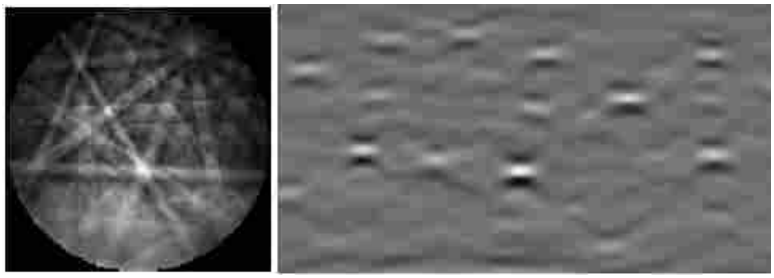

Figure 1.3: An EBSD pattern (left) and its corresponding Hough transform map (right). Each peak in the Hough transform corresponds to a band in the EBSD pattern. Image courtesy of [21].

been developed, but the original, Hough-based techniques dominate the commercial market for EBSD indexing software.

The Hough transform is an integral transform that works by taking a line integral across an image. Each point on the Hough transform represents the line integral across the original image at a certain angle and intersect. Thus, the distinctive band patterns on EBSD patterns show up as peaks on the Hough transform map. An EBSD pattern and its Hough transform are shown in Figure 1.3. Each band corresponds to a diffracting plane in the investigated lattice, and once precisely located, several bands may be used to determine the orientation of the lattice to within about a half a degree [7]. This information may be used to approximate a distortion gradient [16]. This distortion gradient may then be used to resolve dislocation content, as is explained in the next section.

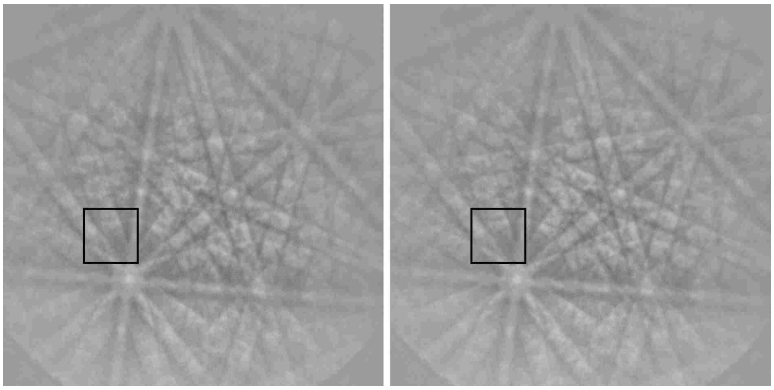

Figure 1.4: Two patterns taken from the same tantalum sample 10 microns apart. Visually, the patterns are very similar. An ROI is marked on both patterns. This pair of ROIs may be used to calculate the shift, $\mathbf{q}$, between them via cross-correlation. Shifts from a number of ROIs may be used to determine the distortion between the two lattices (see Equation 1.9.

However, more recently developed high-resolution EBSD (HREBSD) not only improves the angular resolution of the technique, it also allows strain gradients to be calculated alongside rotations, which lead to more accurate dislocation determination. HREBSD accomplishes this by measuring shifts between regions of interest on related patterns via cross correlation techniques, and subsequently relating these shifts to the relative deformation between the lattices. This allows neighboring points to be directly compared to calculate lattice distortion gradients.

The method works by first defining regions of interest (ROIs) for two images. An example of of ROI selection for two images is shown in Figure 1.4. For each pair of ROIs, a fast Fourier transform convolution is used to determine the shift between the two regions, $\tilde{\mathbf{q}}$. These shifts may then be related to the elastic lattice distortion, β, that would be required to deform the lattice from the first image to approximate the new lattice as follows [14, 23]:

$$\mathbf{q} = \beta\mathbf{r} - (\beta\mathbf{r}\cdot\hat{\mathbf{r}}')\hat{\mathbf{r}}' + (\mathbf{q}\cdot\hat{\mathbf{r}}')\hat{\mathbf{r}}' \tag{1.9}$$

where $\mathbf{r}$ is the vector from the sample origin to the center of the ROI on the phosphor screen, $\mathbf{r}'$ is the vector formed from applying the lattice deformation to $\mathbf{r}$, and $\hat{\mathbf{r}}'$ is the unit vector in the same direction. This geometry is illustrated in Figure 1.5. Once at least four shifts are obtained, Equation 1.9 may be used to determine 8 degrees of freedom of the elastic distortion between the two patterns. The last degree of freedom, the spherical strain, is approximated by assuming zero

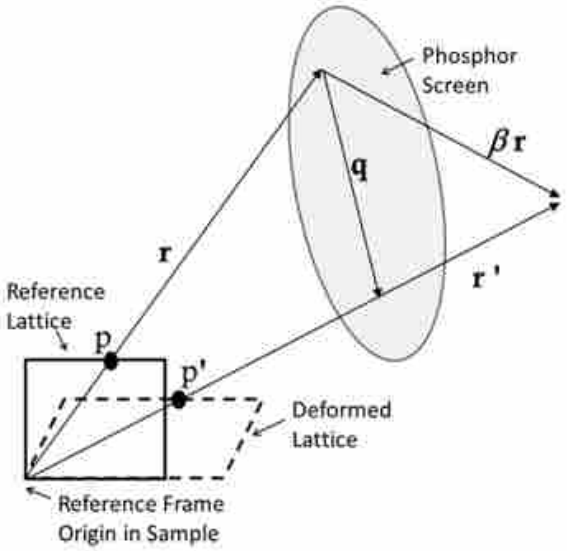

Figure 1.5: Illustration of the vectors involved in relating measured shifts between patterns, $\mathbf{q}$, and the lattice distortion between those patterns, β(see Equation 1.9. Image courtesy of [21]

traction in the distortion [11]. Usually, a large number of shifts are used and the lattice distortion is determined in a least squares sense [24].

It should be noted that HREBSD calculates relative distortion and not absolute distortion between patterns. If EBSD patterns are compared to simulated, strain free patterns of known orientation, then absolute strains are recoverable [23–25]. These methods, however, are highly sensitive to the geometric uncertainty of the diffraction volume, and means of mitigating this error are under development, e.g. [26, 27].

Fortunately, CDM only requires distortion gradients and not absolute distortion. The greater accuracy afforded by comparing neighboring patterns instead of real patterns to simulated reference patterns is preferred when derivatives are desired. Researchers report that HREBSD has a theoretical accuracy to within about 5×10^{-5} when calculating relative distortion between two patterns [12]. Other factors may degrade pattern quality and lead to further decreased accuracy. Properties of the material being examined, microscope settings, dislocation content of the investigated material, polishing technique and EBSD image binning all have an effect on pattern quality.

The relative distortion between patterns collected from neighboring points on a scan may be use to approximate the gradient of the distortion via the forward difference derivative quite

trivially:

$$\frac{d\beta}{dx_i}\Big]_{\vec{p}} = \frac{\beta^{\vec{p},\vec{p}+\Delta\vec{x}_i}}{L} \tag{1.10}$$

where $\vec{p}$ is a location on the surface of a scan, $\Delta\vec{x}_i$ is the vector between the first pattern and an adjacent pattern, L is magnitude of $\Delta\vec{x}_i$, and $\beta^{\vec{p},\vec{p}'}$ is the relative distortion between patterns at location $\vec{p}$ and $\vec{p}'$.

1.3 Background - Continuum Dislocation Microscopy

Once the distortion gradient is obtained via HREBSD, Equations 1.7 and 1.8 may be used to relate the derivatives of lattice distortion, β^e to the dislocation density of individual dislocation systems (from now on, we will refer to β^e simply as β). However, the Nye tensor has at most nine terms (generally less than nine can actually be resolved from the EBSD measurements), whereas most real materials (simple cubic materials being an exception) have significantly more dislocation systems (FCC materials have 18, and HCP materials have 27). Thus, Equations 1.7 and 1.8 are underconstrained when solving for ρ^t. Additional constraints, typically incorporated into some form of optimization approach, must be employed to find a reasonable estimate of dislocation density [13, 16]. The two most common methods involve minimizing the L_2 norm of the individual dislocation densities or the L_1 norm of the dislocation densities . The L_2 method, while having no explicit physical meaning, is very simple to calculate using the pseudo-inverse; the L_1 approach is based upon minimizing total dislocation line length, and therefore total slip.

This paper employs the L_1 norm method. This method is assumed to be more physical because the strain energy of dislocations is often assumed to be a linear function of their length, as predicted by classical equations. While dislocation strain field interactions between dislocations mean that the linear assumption is not necessarily accurate [28], in this study these interactions will be assumed to be negligible, as is typically assumed in the literature. The individual dislocation densities in the L_1 norm may also be weighted according to Schmid factor and/or differences in the critical resolved shear stresses (CRSS) of each slip system in order to better reflect the propensity for a given system to be activated [29] (for example, in magnesium the CRSS of pyramidal systems is many times higher than that of basal systems [30]). If there are multiple Burgers vector lengths in a crystal system, these can also be used to help determine appropriate weighting, as the magnitude

of the Burgers vector is a major factor in the energy of a dislocation. Even in FCC systems, where dislocations are all very similar, different weighting factors have been suggested for edge and screw dislocations [31].

Using the weighted L_1 norm of the dislocation density solution vector as an additional constraint, the problem of determining geometrically necessary dislocation densities on each dislocation system, ρ^t, that can accommodate measured lattice distortion derivatives obtained via EBSD may be stated as:

$$\text{minimize } \sum_{t=1}^{N} |w^t \rho^t|, \text{ s.t. } \alpha = \sum_{t=1}^{N} \rho^t \mathbf{b}^t \otimes \mathbf{v}^t \tag{1.11}$$

where α is obtained via Equation 1.7 and w^t is a weighting factor mentioned above that allows physically more probable slip to be proportionately represented. In this study, weight factors will be set to unity unless otherwise stated. We refer to this set of relationships as the Nye-Kroner method when used to extract dislocation information from lattice distortion derivatives.

While Equation 1.11 is formulated in order to find the most physically likely set of dislocation densities of each dislocation type in a material that can accommodate the measured residual distortion, the equation is more often used as a means of estimating bulk dislocation density (the sum of the individual densities) than as a method of determining accurate values for the individual ρ^t. This is at least partially an acknowledgment that only a fraction of the required degrees of freedom are available to solve Equation 1.11, a problem exacerbated by the fact that lattice derivatives are unavailable in the direction normal to the sample surface. The difficulty in calculating relative activity has led many researchers to find estimates of the overall bulk dislocation density instead of trying to solve Equation 1.11. The entry-wise one-norm norm of α (estimated from its measurable elements only), kernel average misorientation and other techniques have been used to find reasonable estimates of bulk dislocation density [13, 15, 31–33].

1.4 Scope of this work

EBSD dislocation microscopy is a very promising technology for improving our understanding of plasticity for a number of reasons. Sample preparation is minimal, it gathers data at critical length scales, and SEMs capable of collecting EBSD patterns are already almost universal.

However, a few barriers exist to its widespread adoption. This work introduces novel techniques for circumventing these issues. The ambiguity associated with solving the Nye-Kroner relationships (Equation 1.11) and the length scale dependence of the definition of GNDs will both be addressed.

First, in Chapter 2 a new method of estimating total dislocation density without solving Equation 1.11 is developed. The method is subsequently validated using novel dislocation distortion field simulations based on classical dislocation mechanics and applied to a real sample. The bulk dislocation density measurement is applied to an indented single crystal of tantalum. Because of the large number of possible slip planes in a body centered cubic (BCC) material like tantalum, solving the Nye-Kroner equations is highly ambiguous. With the new method, the apparent noise in the bulk dislocation density measurements is significantly reduced.

Secondly, in Chapter 3, the more difficult problem of resolving slip onto individual dislocation systems is addressed. A sample from another study is employed, an indented nickel single crystal. The previous study applied EBSD CDM to the sample by making assumptions about the active slip systems based on the highly constrained deformation it underwent. The results were then validated using crack mechanics and finite element models. In this work we will improve the Nye-Kroner method slightly and validate it via simulation. Then it will be applied to the nickel sample to show that the Nye-Kroner method is robust enough to be applied without assumptions to samples with arbitrary or unknown deformation.

Although the existing Nye-Kroner method is fairly robust, it still fails to adequately capture out of plane deformation in the case of 2D EBSD. Revisiting the simulations from Chapter 2, a new method is derived for directly relating the measured lattice distortion derivatives without the intermediary of the Nye tensor. This method quadruples the number of constraints, significantly reducing the uncertainty of the Nye-Kroner method. This new method is validated through simulation in Chapter 4.

Finally, the issue of length scale as it relates to GND measurements and the definition of GNDs is addressed. Statistical simulations and an experiment with a tantalum single crystal are used to both establish criteria for step size selection for EBSD CDM studies, as well as to show that EBSD CDM can be used to estimate the SSD content of materials, not purely the GND content. This analysis is contained in Chapter 5.

In summary, this paper will present a new method for estimating bulk dislocation density, an improved application of the current Nye-Kroner method which will be validated on real data, a new, more highly constrained way of relating measured lattice information to GNDs, and a method for adequately selecting the step size of an EBSD deformation investigation. These methods are validated using a novel simulation technique based on classical lattice mechanics. The result is a robust set of tools for collecting reliable dislocation information at the mesoscale. These contributions will be further elaborated in the conclusion of this work in Chapter 6.

CHAPTER 2. AN IMPROVED ESTIMATE OF BULK DISLOCATION DENSITY

Equation 1.11 represents the most common way of relating HREBSD information to the dislocation content of a material. As discussed in Chapter 1, application of this equation to extract individual dislocation densities for each dislocation system is non-trivial, due to its under constrained nature for most lattice types (there are at most nine equations for the known Nye coefficients, but the potential for significantly more dislocation types). In the case of simple cubic materials, which have nine unique dislocation systems, Equation 1.8 is exactly determined.

A number of different schemes have been employed to reduce the size of the solution space for Equation 1.8 [13, 16, 29, 34–36]. These include minimizing the L_1 (as in Equation 1.11 and L_2 (Euclidean) norms of the dislocation density solution vector as well as eliminating dislocation types with lower Schmid factors. Such schemes are typically computationally expensive (albeit computation times for resolving dislocation density are often insignificant compared to techniques to calculate the distortion gradients themselves), rely on a number of assumptions, unreliably detect dislocation content associated with out-of-plane deformation, and convergence of the algorithm may be sensitive to the starting point. Hence it is convenient to develop methods of estimating total dislocation density that do not rely on solving Equation 1.8.

Sun, et al. point out that for the case of simple cubic materials (where there are only nine orthogonal dislocation types), there is a one-to-one correspondence between the components of the Nye tensor and the dislocation densities, ρ^t, when an appropriate reference frame is chosen [16]. For more complex crystal systems, the simple cubic deconstruction acts as an approximate lower bound for dislocation density. This lower bound may be used as an estimate for the total, or bulk, dislocation density. El-Dasher, et al. showed that the entry-wise one-norm of the α tensor is proportional to the geometrically necessary bulk dislocation density in an FCC material [13].

Equations 2.1 and 2.2 summarize these relationships:

$$\|\alpha\|_1 = \sum_i \sum_i |\alpha_{ij}| \tag{2.1}$$

$$\rho \approx \frac{1}{b}\|\alpha\|_1 \tag{2.2}$$

Note that Equation 2.2 is precisely true in the case of simple cubic materials and that Equation 2.1 is the definition of the entry-wise one-norm of α. Note that this estimate does not involve solving for or minimizing the norm of the vector of dislocation densities of each type, ρ^t, in Equation 1.8. Rather, this method uses a norm of the Nye tensor itself to estimate the bulk dislocation density. However, even these estimates are difficult to apply, because most EBSD is done on a sample surface, meaning a third of all lattice distortion derivatives are unavailable, meaning only three terms of the Nye tensor may be unambiguously recovered. This 2D problem is discussed further in Section 2.1.

This chapter will justify the use of Equation 2.2 as a means of estimating bulk dislocation density for more complex crystal lattices, discuss various estimates of the entry-wise one-norm of α based upon only those components that can be recovered from HREBSD. The results will be validated using a novel dislocation field simulation based on classical equations for distortion fields around dislocations adjusted for a continuum view. Furthermore the sensitivity of the solution to the orientation of the dislocations relative to the sample surface. Finally, this method of estimating dislocation density will be applied to actual EBSD data from a deformed single-crystal of tantalum, where it results in significantly reduced noise.

2.1 Estimates of the entry-wise one-norm of the Nye tensor

FCC crystals have 18 unique dislocation systems, but Equation 1.8 provides at most 9 constraints, if derivatives were taken in 3 orthogonal directions. However, EBSD is fundamentally a surface characterization technique, resulting in known gradients in only two directions. Methods have been developed for taking derivatives in the sample normal direction, e.g. via focused ion beam sectioning [32, 34], but generally these methods are expensive, have poor resolution, are time-consuming, or destroy the sample, making *in situ* tests impossible [20]. Hence, only 12 of

the 18 necessary distortion derivatives required by Equation 1.7 can be readily obtained; only the rightmost column of α (the α_{i3} terms) can be fully recovered. Wheeler, et al point out that these terms of the Nye tensor (α_{i3}) represent the net Burgers vector for a circuit in the sample plane, and allow the extraction of some out-of-plane deformation information if additional constraints are imposed [28]. The one norm of the fully known α_{i3} column can be used as an approximation for the full Nye tensor.

If strain is neglected (e.g. [28, 37]), then two additional terms are available, as well as one extra constraint [38]. The available components of α from surface HREBSD techniques are illustrated by expanding Equations 1.7 in terms of the strain (ε) / rotation ω components of β, as seen in Equation 2.3. Strain and rotation are separated from distortion assuming infinitesimal strain, meaning that ε and ω are the symmetric and antisymmetric parts of β, respectively.

$$\alpha = \begin{bmatrix} \tilde{\varepsilon}_{12,3} + \tilde{\omega}_{12,3} - \varepsilon_{13,2} - \omega_{13,2} & \varepsilon_{13,1} + \omega_{13,1} - \tilde{\varepsilon}_{11,3} & \varepsilon_{11,2} - \varepsilon_{12,1} - \omega_{12,1} \\ \tilde{\varepsilon}_{22,3} - \varepsilon_{23,2} - \omega_{23,2} & \varepsilon_{23,1} + \omega_{23,1} - \tilde{\varepsilon}_{21,3} - \tilde{\omega}_{21,3} & \varepsilon_{21,2} + \omega_{21,2} - \varepsilon_{22,1} \\ \tilde{\varepsilon}_{32,3} + \tilde{\omega}_{32,3} - \varepsilon_{33,2} & \varepsilon_{33,1} - \tilde{\varepsilon}_{31,3} - \tilde{\omega}_{31,3} & \varepsilon_{31,2} + \omega_{31,2} - \varepsilon_{32,1} - \omega_{32,1} \end{bmatrix} \tag{2.3}$$

Terms with unavailable derivatives (i.e. gradients in the direction normal to the surface) are marked with a tilde. Since diagonal terms of the rotation tensor are zero, there are 30 remaining terms in the expanded representation. The missing α components limit the number of constraints available in Equation 1.11, and further complicate the recovery of relative dislocation activity.

As seen in Equation 2.3, if strain is neglected, 2 additional terms become available to solve Equation 1.11, the rotation terms in the (1,2) and (2,1) positions (which employs a total of six non-zero rotation terms). The difference of the measurable rotations in the (1,1) and (2,2) positions provides a sixth constraint, utilizing a total of eight non-zero rotation terms from Equation 2.3. This suggests another possible approximation of the entry-wise one-norm of α based solely on 2D orientation-based EBSD; i.e. the sum of the absolute values of the five approximated α terms: α_{13}, α_{23}, α_{33}, α_{12} and α_{21} (the α_{11} - α_{22} term, or sixth constraint, cannot be used because it is a difference of terms).

Finally, we posit a third estimate of the entry-wise one-norm of the Nye tensor, assuming all unknown derivatives are zero to approximate all nine terms of α, and then utilizing all nine

approximated terms to estimate the one-norm. Although this estimate does not rely on any fundamental assumptions, it includes the most possible information, and we demonstrate that it is a superior estimate through simulation. These approximations must be scaled because the available terms represent only a fraction of the whole entry-wise one-norm; the scaling factor is discussed below.

2.2 Dislocation density field simulations based on classical lattice mechanics

In order to assess the accuracy of a given approximation, accurate relationships for elastic distortion (as would be measured by EBSD) are required for a given assumed dislocation content. Greens function formulations [39–42] are available for determining elastic distortion for both discrete and continuous fields of dislocations. The continuous formulation is compatible with our goals in this paper, but the integration can be time consuming and prone to numerical error. Hence a different approach is taken.

The traditional analytic relations between dislocation types and distortion are well-suited for numerical calculation purposes, but are formulated for discrete dislocations and lead to zero curl of the distortion (and hence, a null Nye tensor). If the gradient of the analytically defined displacement is taken to arrive at the elastic distortion, and the curl of the resultant distortion field is derived, the result is identically zero (apart from across singularity points).

In order to apply the analytical model to a continuum level dislocation field, classical distortion fields around dislocations were taken from Lazar [43] (not including the non-linear terms) and then smeared over the simulated region of interest; i.e. they were modeled as if a dislocation field were comprised of an infinite number of dislocations with infinitesimally small Burgers vectors, resulting in the same net Burgers vector per unit area as the discrete case.

Assuming that the z direction lies along the dislocation line, the x direction is in the direction of the Burgers vector and the y direction is perpendicular to the slip plane, the analytic equations for the non-zero distortion terms around an edge dislocation in a linear elastic isotropic

medium are:

$$\beta_{xx} = -\frac{b}{4\pi(1-\nu)}\frac{y}{r^2}\left((1-2\nu)+\frac{2x^2}{r^2}\right) \text{ where } r^2 = x^2+y^2 \tag{2.4}$$

$$\beta_{xy} = \frac{b}{4\pi(1-\nu)}\frac{x}{r^2}\left((3-2\nu)+\frac{2y^2}{r^2}\right) \tag{2.5}$$

$$\beta_{yx} = -\frac{b}{4\pi(1-\nu)}\frac{x}{r^2}\left((1-2\nu)+\frac{2y^2}{r^2}\right) \tag{2.6}$$

$$\beta_{yy} = -\frac{b}{4\pi(1-\nu)}\frac{y}{r^2}\left((1-2\nu)+\frac{2x^2}{r^2}\right) \tag{2.7}$$

where b is the length of Burgers vector and ν is Poissons ratio. If a continuous field of edge dislocations is assumed, with line directions in the z-direction, that occupies an infinite rectangular column between $x = s$ and $x = t$, $y = p$ and $y = q$, then the resultant β_{xx} distortion (for example) at a point x_0,y_0 (for any z) is given by:

$$\beta_{xx} = -\frac{b}{4\pi(1-\nu)(t-s)(q-p)}\int_{y=p}^{q}\int_{x=s}^{t}\frac{y_0-y}{r_0^2}\left((1-2\nu)+\frac{2(x_0-x)^2}{r_0^2}\right)dxdy$$

$$\text{where } r_0^2 = (x_0-x)^2+(y_0-y)^2 \tag{2.8}$$

Then the distortion components for the edge dislocation field depend upon being able to work out two integrals (calculated using Maple) [44]:

$$\int_{y=p}^{q}\int_{x=s}^{t}\frac{y_0-y}{r_0^2}dxdy = I(q,t)-I(q,s)-I(p,t)+I(p,s) \tag{2.9}$$

where $I(q,t) = (x_0-t)\frac{\ln\left((y_0-q)^2+(x_0-t)^2\right)}{2} - (y_0-q)\tan^{-1}\left(-\frac{(x_0-t)}{(y_0-q)}\right)+t$

and

$$\int_{y=p}^{q}\int_{x=s}^{t}\frac{(y_0-y)(x_0-x)^2}{r_0^4}dxdy = J(q,t)-J(q,s)-J(p,t)+J(p,s) \tag{2.10}$$

where $J(q,t) = -\frac{(y_0-q)}{2}\tan^{-1}\left(-\frac{(x_0-t)}{(y_0-q)}\right)+\frac{t}{2}$

For a discrete screw dislocation (with line vector in the z direction), the distortions are given by:

$$\beta_{zx} = -\frac{b}{2\pi}\frac{y}{r^2}, \beta_{zy} = -\frac{b}{2\pi}\frac{x}{r^2} \tag{2.11}$$

and the distortions from a continuous field are obtained similarly to those for the edge dislocation (using the same integrals given in Equations 2.9 and 2.10). It was assumed that mixed fields of dislocations could be modeled by summing the combined distortion fields of edges and screws using the principle of superposition.

When numerical derivatives of these simulated distortion fields were used to calculate α using Equation 1.7, they were equivalent, within numerical error, to α calculated via Equation 1.8, demonstrating the validity of this method.

In order to validate various methods of extracting dislocation information from EBSD data, the numerical fields in this section were used to simulate the measurable lattice distortion of a given dislocation structure. First, a subset of dislocation systems are selected and assigned a dislocation density. The elastic distortion fields for each dislocation type are simulated via the smearing technique presented in this section over a cubic volume with side length analogous to the step size of an actual scan. These fields are then rotated into the sample frame. The bulk GND density of such a simulation is given by $\sum_t |\rho^t|$.

Distortions measurable via the various EBSD approaches were determined by taking a numerical gradient across the surface of the simulated cube, and the Nye tensor was calculated using Equation 1.7 (also given in expanded form in Equation 2.3). The bulk GND content was then estimated from the Nye tensor by one of the methods under examination in this paper, and the result compared to the actual density. The results of these simulations are presented in the subsequent sections.

2.3 Accuracy of the GND quantification using a typical minimization scheme

For comparison with an entry-wise norm approach to estimating GND density (Equation 2.2) presented in this paper, a typical version of a minimization method for estimating dislocation density (1.11) was applied to the simulated fields discussed in Section 2.2. A series of random GND fields were simulated for a cubic volume of interest with side length 100 nm. Two tests

randomly selected subsets of five and fifteen dislocation systems, respectively, from all possible pure edge or screw dislocations for the material lattice type at each point. For the test case, nickel, an FCC material, was simulated. The lattice was given a random orientation relative to the global frame. The dislocation density of each randomly selected dislocation systems was set to $1 \times 10^{14} m/m^3$, resulting in total dislocation densities of $5 \times 10^{14} m/m^3$ and $1.5 \times 10^{15} m/m^3$, respectively.

The distortion fields were then calculated as discussed in Section 2.2 for each dislocation system, and then superimposed. The measured GND content was determined by inserting only the measurable Nye tensor constraints, as elucidated by Pantleon, (α_{13}, α_{23},α_{33},α_{12}, α_{21}, and $\alpha_{11} - \alpha_{22}$) into Equation 1.11. The problem was solved with a gradient based optimization algorithm using the origin (zero dislocation density of all types) as the starting point. The L_1 norm (sum of the absolute values) of the resulting solution vector of dislocation densities was calculated to determine the measured bulk dislocation density. This process was repeated for 2000 simulated volumes.

While there was significant variance in the results, depending upon the GND type, this approach resulted in a GND approximation that was on average 65.9% of the actual value. The distribution of the measured bulk dislocation density was normal with a standard deviation of 28%. We will not discuss this method further in the current paper, but will turn our attention to the entry-wise one-norm approach that is both much easier to apply, and is generally less sensitive to dislocation type.

2.4 Norms of the Nye tensor for estimating GND density

One method for estimating dislocation, based on the entry-wise one-norm of α, has already been suggested in Equation 2.2. Our first task is to determine whether the entry-wise one-norm of the Nye tensor provides a reasonable approximation of the bulk GND density if the full Nye tensor is available. For a simple cubic lattice, the entry-wise one-norm method is equivalent to solving Equation 1.11 for ρ^t and then summing the absolute values of the terms, resulting in the correct dislocation density. For other lattice types this approach results in only an approximation to the overall dislocation density.

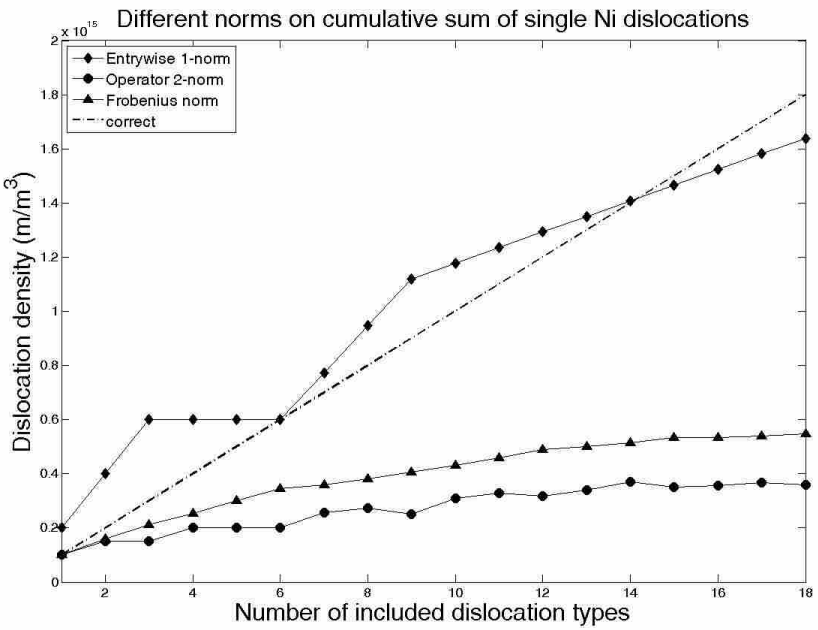

Figure 2.1: The relationship between various approximations of bulk dislocation density and the actual dislocation density in a simulated dislocation network as each of the 18 unique dislocation systems of nickel (FCC) are added to a cumulative GND field.

Based upon inspection of Equation 1.8, the entry-wise one-norm of α is related to the dislocation density, ρ by a factor of $1/b$, where b is the length of the Burgers vector. In the case of a non-cubic material, such as HCP magnesium, the magnitude of the Burgers vector varies by dislocation type, and an average Burgers vector length (or weighted average, if something is known about the relative content of various dislocation types) must be used in Equation 2.2. Hence this method is perhaps least suited to materials with variable Burgers vector length, such as those with a hexagonal lattice. To demonstrate the robustness of the approach, HCP magnesium will be used as an example material, along with a conventional FCC material in the next section.

The relationship between the complete entry-wise one-norm of α (divided by the average magnitude of the Burgers vector) and the actual bulk dislocation density for a cumulative field of dislocations in Ni, an FCC material, is plotted in Figure 2.1; the initial field has a single dislocation type of density $1 \times 10^{18} m/m^3$, and subsequent fields (numbered along the x-axis) are created by addition of a further dislocation type (with equal density). For comparison, the standard operator 2-norm and Frobenius norm of the Nye tensor are also plotted, with definitions given in Equations

2.12 and 2.13, respectively.

$$\|\alpha\| = \max \{\|\alpha \mathbf{n}\| : \mathbf{n} \in R^3 \text{ with } \|\mathbf{n}\|\} \tag{2.12}$$

$$\|\alpha\|_F = \sqrt{\sum_i \sum_j \alpha_{ij}^2} \tag{2.13}$$

Note that in Equation 2.12, the norm operator on the right hand side is the standard Euclidean vector norm, but on the left hand side, it is the induced Euclidean matrix norm, as is conventional.

With only one dislocation type, the operator 2-norm is the best approximation. However, with an appreciable number of dislocation types, the entry-wise one-norm method is a reasonable approximation of bulk dislocation density based on the Nye tensor. It is clearly superior to the other norms examined. For the remainder of this study, the entry-wise one-norm of the full Nye tensor will be assumed to be an accurate approximation of geometrically necessary dislocation density. Various approximations based upon an incomplete Nye tensor, for the different EBSD-related levels of incompleteness described above, will be assessed against the full entry-wise one-norm.

2.5 Estimating GND density from an incomplete Nye tensor

Since standard EBSD techniques can only recover distortion derivatives in two directions, not all of the terms of α are known (see Equation 2.3), and the full entry-wise one-norm must be approximated using the known terms. Once the norm is approximated, an estimate for dislocation density may be found using Equation 2.2.

The first approximation that we test uses the right hand column of the Nye tensor, without the strain components. As discussed above, if strain is to be neglected, one may in fact accept five terms of the tensor as being reasonably accurate [38]. Pantleon also points out that neglecting strain in Equation 2.3 makes $\alpha_{11} - \alpha_{22}$ available in addition to the five other terms. This last constraint is useful for minimization schemes; but because the entry-wise one-norm approach presented here requires the magnitude of the terms of the Nye tensor, only the five terms (α_{13}, α_{23},α_{33},α_{12}, and α_{21}) are used to estimate the norm of the Nye tensor in our second approach. Adding the strain

terms available from HR-EBSD techniques (and assuming this strain is significant), gives three fully known α terms (α_{13}, α_{23},α_{33}) which may be used as the basis for another estimate of dislocation density. Furthermore, using the five term approximation without neglecting strain results in a fourth approximation. Finally, a fifth approximation was examined that used all measurable strain and rotation terms in Equation 2.2 - a nine term approximation. This estimate includes the known parts of all terms of the alpha tensor in Equation 2.3 while unknown distortion derivatives were neglected.

In order to test the impact of these five different approximations of α on the calculated entry-wise one-norm (i.e. on the estimated bulk GND density), α was calculated for the test GND fields using all the known terms in Equation 2.3; the unknown terms (marked with a) were ignored. The three-term estimate of the entry-wise one-norm was then calculated by summing the absolute values of α_{13}, α_{23}, and α_{33} with and without the strain components. The five-term estimates were calculated in the same way, with the addition of the absolute value of α_{12} and α_{21} (with and without the strain components). The nine term estimate first approximates each term of the Nye tensor with what derivative terms are known, and then the sum of their absolute values is evaluated as before. Thus, each estimate includes more and more known strain and rotation terms.

Because these approximations of the entry-wise one-norm do not include all the necessary Nye tensor components (or in the case of the nine term approximation, Nye components estimated from incomplete information) they need to be corrected by some factor to arrive at a reasonable estimate for GND density. For the conventional EBSD methods (strain is ignored, but the accuracy is assumed to be the same), this factor was empirically determined via simulations; the best scaling factor turned out to be 5.5 for the three term approximation and 3.6 for the five term approximation. This contradicts the general assumption that this factor should be 3 for estimates of bulk dislocation density using the three terms of the rightmost column of α. For the HREBSD methods (those which included strain) the appropriate scaling factor was found to be given by the total number of non-zero components in Equation 2.3 (i.e. 30) divided by the number of components included in the approximation. For example, the rightmost column has 10 of the 30 non-zero components, so the three term estimate must be corrected by a factor of $30/10 = 3$. Likewise, the five-term approximation must be corrected by a factor of $30/14 = 2.14$, and the nine-term estimate by a factor of $30/20 = 1.5$. This result suggests that, based on the distortion fields simulated, each

strain and rotation gradient term has a roughly equal contribution to the total dislocation density for the simulated fields.

To evaluate the performance of these approximations, dislocation fields were simulated for a cubic volume of interest with side length 100 nm. An FCC (Cu) and an HCP (Mg) material were examined. FCC materials have 18 unique dislocation systems and HCP materials have 27 unique dislocation systems. The same test GND fields as described in Section 2.3 were simulated. The distortion fields were then calculated as discussed in Section 2.2, and various estimates of dislocation density were calculated as explained. Then the ratio of each of these estimates (including the correction factor) to the correct GND density was calculated. This ratio of recovered to simulated dislocation density was averaged at 2000 different grain orientations. For Cu, only full dislocations (with Burgers vectors in the $[110]$ family) were considered (Shockley partials were ignored). For Mg both the $\langle$a$\rangle$ type and $\langle$c+a$\rangle$ type dislocations were considered.

For all five of these approximations, the average ratio of recovered density to simulated density was unity to within numerical error. This is not surprising because the scaling factor for each approximation was chosen to give such a result. However, the result demonstrates the validity of the one-norm of α as a means of estimating dislocation density assuming that the correct correction factors are applied to compensate for the unknown distortion derivative terms.

However, the orientation of the dislocations relative to the sample surface can have a drastic effect on the recovery of the dislocation density. For example, an edge dislocation parallel to the sample surface results in an α tensor with zeros in the rightmost column; hence the three term approximation would result in prediction of a null dislocation field. The more terms of α are used to estimate its one-norm, the lower the chances of a dislocation structure arbitrarily oriented relative to the sample surface being misrepresented due to orientation effects. Thus, for arbitrary dislocation fields, the more distortion derivative terms used in the estimate of dislocation density, the greater the likelihood of the appropriate dislocation density being represented in the estimate.

The one-norm approximations of α must be compared based on their ability to consistently estimate dislocation density regardless of orientation effects. Because the orientation and dislocation content of these simulations was random, and the error is a function or orientation, error from simulation to simulation was normally distributed. Thus, the standard deviation of these estimates

is a better metric for evaluating their performance. The standard deviations of each of these five estimates are given in terms of percent difference from the actual GND density in Table 2.1.

Looking at the standard deviation of the estimates shows significant disparity in performance. As more strain and rotation terms (based upon distortion derivative terms) are added, the estimates experience less sensitivity to the orientation of the dislocations to the sample surface, making the nine-term approximation a superior general estimate of the dislocation density of a sample, as expected. Orientation sensitivity is described more in Section 2.6.

Surprisingly, the three and five term estimates that used conventional EBSD (no strain) had very similar accuracy to their HREBSD counterparts (once correctly scaled) despite using less available information. However, the nine term approximation, to which there is no conventional EBSD analogue, performed the best, being more likely to be more accurate for an arbitrary dislocation structure. Consideration of conventional EBSD approximations will be omitted in later sections for brevity, and only HREBSD approaches will be considered (the HR-EBSD estimates of the one-norm of α only differ in that they assume strain to be significant).

It should be noted that the accuracy of this method on non-cubic materials like magnesium, which is HCP, is dependent on the selection of an average Burgers vector. The method works well in simulation, where the average relative amounts of each dislocation type are approximately random. In reality the relative amounts of $\langle$c+a$\rangle$ slip to $\langle$a$\rangle$ slip is unknown and often a quantity that the observer would like to measure. However, if bulk dislocation density is the only quantity sought, the estimate will not be off by more than a factor of about 2 for magnesium because a $\langle$c+a$\rangle$ dislocation Burgers vector is approximately twice as long as that of an $\langle$a$\rangle$ type dislocation. The relative length of the $\langle$c+a$\rangle$ Burgers vector and the relative amount of slip can vary depending on material. Many estimates for the relative amount of $\langle$a$\rangle$ and $\langle$c+a$\rangle$ slip in magnesium exist in the literature (e.g. [30]). Considering the large difference between FCC and HCP systems and the fact that the entry-wise one-norm dislocation density method worked well for both of them, it is assumed that this method will serve as a good approximation for most crystal systems, especially other cubics (e.g. the BCC real example studied below).

2.6 Orientation sensitivity

When using approximations for dislocation density, as presented above, it is important that users are aware of the factors affecting the accuracy of the estimate. As already discussed, accurate recovery of the dislocation density tensor is strongly dependent on the orientation of the dislocation(s), and therefore dependent on the crystal orientation relative to the sample surface. For a highly textured material, or within a given grain, the predominant dislocation type may be oriented such that certain components of the Nye tensor contain a disproportionate weight compared to the rest of the tensor, resulting in poor dislocation density estimates via the scaling approach to the entry-wise one-norm.

Similarly, it may be that certain dislocation types (for example, those with shallow angles relative to the sample free surface) may be more highly affected by the sample preparation process than others (for example, they may escape to the free surface more easily), leading again to under-represented terms in the tensor.

In order to quantify the effect of crystal orientation on the estimated dislocation density, five random dislocation types are chosen for an Cu sample, and the estimate of dislocation density using the three methods described above is compared while rotating the lattice orientation about a vector in the free surface. The ratio of the estimated GND density to the actual density, as a function of the angle of rotation from the surface, is plotted in Figure 2.2 for the three different estimates.

Once again, the performance of the nine-term estimate is superior to the other two. The potential error is related to the standard deviation calculated in Table 2.1.

Note that up until this point, the composition of the dislocation structure has always been modeled as random, where each dislocation system is independent of each other and of any macroscopic effects, such as deformation. This has been done to show that these methods work generally on arbitrary dislocation structures. Incorporating known biasing effects of deformation via crystal plasticity modeling and/or orientation has the potential to make these estimates more accurate.

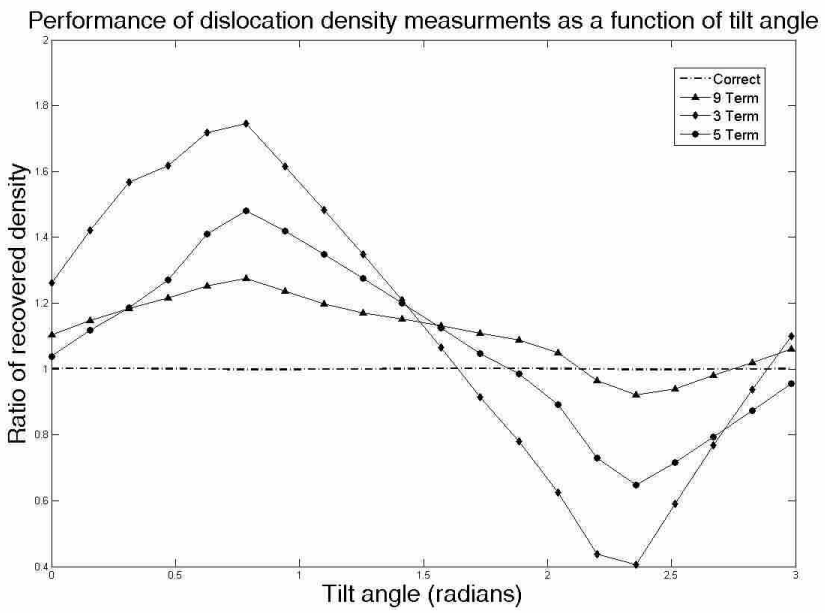

Figure 2.2: Dislocation density recovery ratio as a function of tilt angle relative to the sample surface (Φ) for a random network of 9 dislocations. The simulated material is copper (FCC).

2.7 Performance on a real scan

In order to show that entrywise one-norm estimates of dislocation density that include more terms introduce less variance, the three methods were also compared on actual HR-EBSD scan data. A sample of single crystal tantalum was deformed using a wedge indentation at room temperature by researchers at Columbia University (Jeff Kysar, et al.). The indenter had a 90° included angle, and the line load was applied to the $(0\ 1\ 2)$ face of the crystal in the $[0\ 2\ \bar{1}]$ direction. The sample was then cut in half parallel to the $(0\ 2\ \bar{1})$ plane via EDM. BCC materials, like tantalum, have a number of possible slip planes at room temperature, making Eq. 1 quite under-constrained and difficult to apply. The entry-wise one-norm approach can be applied easily. The sample was polished with oil-based diamond suspensions starting from a particle size of 9 m to 1 m. After being ultrasonically cleaned in ethanol, the sample was etched with a 50% H_2SO_4,25% HO_3, 25% HF volumetric solution at 18-20° C. A 1 mm $\times$ 1 mm square area of the sample around the indentation was scanned in a FEI Helios NanoLab^{TM} 600i scanning electron microscope using TSLs OIM^{TM} software and a high speed Hikari^{TM} camera to gather EBSD patterns. The step size

between patterns collected was 2.5 microns. Standard EBSD geometry and an accelerating voltage of 25 keV were used. The binning size of the pixels on the phosphor screen was 2×2.

The distortion derivatives were calculated using the HREBSD cross-correlation techniques between adjacent patterns as described earlier. For more details, see section 3.2 of [14]. The entry-wise one-norm of the Nye tensor was approximated in the three ways discussed previously: using the three fully recovered terms (the conventional method), adding the partially known α_{12} and α_{21} terms, and using all available β derivative terms. The entry-wise one-norms of each of these approximations were then scaled by the inverse of the theoretical ratio of recovered information (3, 2.143, and 1.5, respectively) and the Burgers vector of Ta. These three results were plotted in Figure 2.7. The dislocation density is plotted in log units of m/m^3.

As expected from the simulated dislocation density networks, the variance in the dislocation density decreases as more β terms are employed, while the contrast and sharpness of the images increases. This variation in noise between the images was quantified by using two-dimensional discreet Fourier transforms of the images. The average of the magnitude of the complex low frequency terms was divided by the average of the magnitude of the high frequency terms to provide a signal-to-noise ratio. Krieger Lassen developed similar image metrics based on the discreet Fourier transform to gauge image quality of EBSD images in [45].

It should be noted that lower noise does not necessarily correspond to a better representation of reality. If the sample has fine periodic structure, this structure would be interpreted as noise, and thus care must be taken when defining the transition from signal to noise. The cutoff between signal and noise was selected such that the maximum wavelength considered noise was 3 pixels, less than the wavelength of the visible periodicity of the sample (about 4-5 pixels). This cutoff wavelength parameter was adjusted to see how the results were sensitive to it. The signal-to-noise ratios themselves were highly sensitive to the cutoff wavelength, but the relative magnitudes of the signal-to-noise ratio for each of the approximations were very consistent. Results are shown in Table 2.2.

Based on the discreet Fourier transform of the different images, the three term approximation has a 18% lower signal-to-noise ratio than the nine term approximation and the five term approximation has an 7% lower ratio. The higher signal-to-noise ratio of the nine-term method indicates less noise in the characterized GND field. This difference in noise coincides with the

results of the simulations presented, supporting the idea that the addition of more terms increases the accuracy of the dislocation density estimate.

2.8 Conclusions

In most cases, only a limited number of Nye tensor terms are made fully available via HR-EBSD dislocation microscopy because distortion derivatives are not accessible in the direction normal to the sample surface without sectioning or other costly and time consuming 3D techniques. This limits the ability to recover the full Nye tensor and corresponding bulk dislocation density. A robust and convenient method for estimating bulk dislocation density (ρ) has been proposed, namely Equation 2.2.

Because of the missing β derivatives, the entry-wise one-norm of the full tensor must also be estimated based upon available tensor components. Five such approximations were evaluated. The most accurate method utilizes estimates of all the terms of the Nye tensor derived from all known distortion derivatives obtained from HREBSD. As shown in the simulations, this estimate must be corrected by a factor of 1.5 to account for missing terms in the tensor, based upon the assumption that the dislocation structure is random. This approximation for the GND density showed the least amount of variation relating to dislocation type and crystal orientation in the simulations. When applied to actual scan data, the resultant dislocation density map displayed a higher signal to noise ratio compared to the maps derived from a lower number of Nye tensor terms.

This method is a convenient approximation for the GND density of a material because it may be naively employed without any assumptions as to stress state or active slip systems. Computationally, it is much more efficient than minimization schemes. For greater accuracy, estimates of the dislocation density may be adjusted based on the orientation of the dominant dislocation types relative to the sample surface.

Continuum dislocation microscopy is still a developing field. The method presented here provides a simple approximation of bulk dislocation density, but is limited in that it does not resolve that density onto specific dislocation systems. The rest of this work presents methods of fully resolving dislocation density by controlling the level of error and dealing with the under-constrained nature of Equation 1.11 when bulk estimates are unsatisfactory.

Table 2.1: Standard deviation of the percent error of various estimates of the GND density given by the Nye tensor.

Approximation	Standard deviation, Cu	Standard deviation, Mg
3 terms (no strain), 5 $\perp$	38.1%	41.4%
5 terms (no strain), 5 $\perp$	25.7%	27.8%
3 terms, 5 $\perp$	38.4%	47.4%
5 terms, 5 $\perp$	25.8%	30.9%
9 terms, 5 $\perp$	13.1%	14.7%
3 terms (no strain), 15 $\perp$	37.3%	39.1%
5 terms (no strain), 15 $\perp$	25.1%	26.6%
3 terms, 15 $\perp$	36.5%	43.2%
5 terms, 15 $\perp$	25.1%	28.8%
9 terms, 15 $\perp$	12.5%	14.1%

Table 2.2: Comparison of the noise for estimates of dislocation density via the entry-wise one-norm.

Approximation	**Signal-to-noise**
Three-term	1.07
Five-term	1.21
Nine-term	1.30

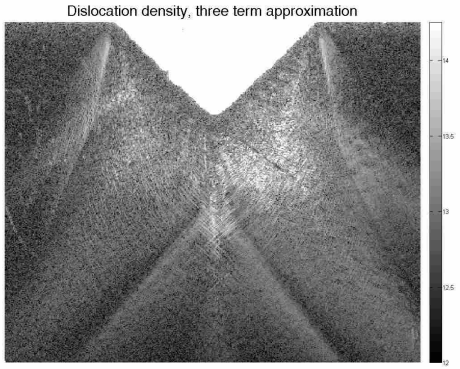

(a)

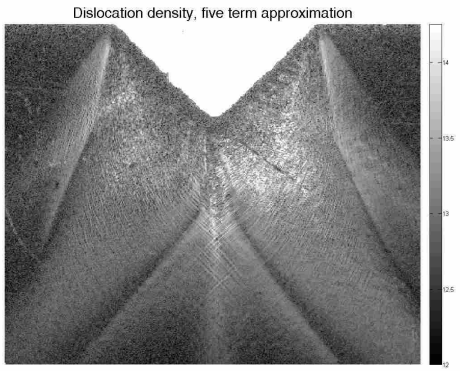

(b)

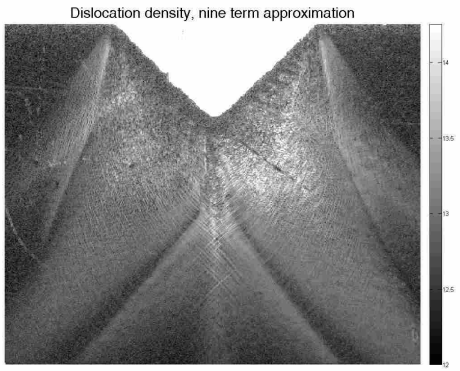

(c)

Figure 2.3: Dislocation density in common log units of m/m^3 around a micro-indentation in a single crystal tantalum sample according to the (a) three-term, (b) five-term and (c) nine-term approximations.

CHAPTER 3. ROBUST APPLICATION OF THE NYE-KRONER EQUATIONS TO RESOLVE DISLOCATION CONTENT ONTO INDIVIDUAL SLIP SYSTEMS

In Chapter 2, a method was presented to estimate the total dislocation density of a material without solving the conventional CDM equation, Equation 1.11. This estimate is valuable because of the missing Nye tensor terms and because even under ideal circumstances, this equation is highly under constrained (as is particularly the case for BCC materials, like tantalum). However, in the case of FCC materials, which only have 18 unique slip systems, it is valuable to be able to resolve the dislocation content onto individual dislocation systems.

Because of the ambiguity associated with solving the CDM equation, researchers rarely report dislocation densities on individual slip systems due to lack of validation. One exception is the work of Kysar, et al. [29, 36, 46, 47]. Kysar's research group used CDM to examine a well understood deformation type, plane strain around a nanoindenter (analogous to a propagating crack). Making a number of assumptions that simplified Equation 1.8 to a fully constrained, 3 degrees of freedom problem, this research group detected the dislocation types predicted by crack mechanics [48, 49] and their own finite element models.

Kysar's research provided valuable validation for EBSD CDM's ability to resolve dislocation density onto individual slip systems, but the number of additional constraints and assumptions required is impractical for general use. The dislocation field simulations presented here in Section 2.2 provide an opportunity to validate the the use of Equation 1.11 without the use of additional constraints. This chapter employs dislocation field simulations to validate and improve the Nye-Kroner equations of CDM when applied without prior knowledge of the deformation of the material. Finally, the improved equations are applied to Kysar's indented nickel single crystal sample to show that assumptions are not necessary to resolve dislocation density onto individual slip systems.

3.1 Optimization methods

Equation 1.11 is the standard method of resolving, and its development was thoroughly explained in Chapter 1. However, one issue that has not yet been addressed, is the manner of performing the optimization. The solution space for this optimization problem is quite complex, and navigating it is non-trivial.

According to Equation 2.3, only 3 terms of the Nye tensor (and thus 3 constraints for Equation 1.11) are obtainable in 2D HREBSD. However, as referenced previously, if strain is assumed to be negligible, then there are actually three additional constraints available, namely the α_{12} and α_{21} terms as well as the difference between α_{11} and α_{22} [38]. This six-constraint method utilizes a total of eight non-zero rotation terms from Equation 2.3, whereas the 3 term method only uses four.This paper will apply both sets of constraints on Equation 1.11, the set of three and the set of six, to simulated distortion fields of continuum dislocation fields and real data in order to demonstrate the robustness of the Nye-Kroner method and the relative advantage of using 6 constraints instead of 3.

Thus, for the assumed FCC material, Equation 1.11 represents an optimization problem with the 3 or 6 linear constraints and 18 unknowns (FCC materials have 18 unique combinations of dislocation line vector and Burgers vector). On the surface, Equation 1.11 appears to be a simple linear programming problem, i.e. the objective function and constraints are all linear. Linear programming problems are convenient because the Kuhn-Tucker [50] conditions may be used to solve directly for the optimum. However, the discontinuities associated with the absolute value function mean that there are a large number of potential minima ($2N$, where N is the number of dislocation types), making direct calculation impractical and gradient based optimization problematic because of high sensitivity to initial position.

To circumvent this problem, multiple approaches were examined. First different starting points were attempted with gradient based optimization. Of the available starting points, two were selected as representative: the L_2 norm (least squares) solution (which may be easily calculated), and the point where all dislocation densities were zero (the origin). Besides a gradient based method, a stochastic optimization algorithm was also employed, namely particle swarm optimization [51]. However, using gradient based methods with the least squares solution as the starting

point proved to reach the global optimum very consistently, obviating the need for computationally expensive stochastic optimization.

In considering the choice of starting point, something interesting was observed. When the algorithm is applied using the L_2 norm starting point, and the global optimum is reached, the Nye-Kroner method can sometimes precisely predict both the magnitude and type of dislocation content; but if the dislocations are not oriented favorably, Nye-Kroner completely misses the dislocation content or mistakes the dislocation type. However, when the origin is used as the starting point, the local optimum that the algorithm comes to tends to predict the correct dislocation type more frequently, albeit at the wrong magnitude and with noise on the other dislocation types.

The Nye-Kroner method is implemented in four ways, using 3 and 6 constraints and using the origin or the least squares solution as the starting point for the gradient based optimization algorithm. Once the optimal implementation of this technique is determined via simulation, it is subsequently applied to a real sample.

3.2 Validation via simulation

Based upon the approach described in Section 2.2, simulated volume elements were generated with known dislocation content. The simulated material, nickel, was selected to be compatible with the real data set described in the next section. As an FCC material, it has 12 slip systems, each of which may be of edge or screw character. In reality, nearly all dislocations are of mixed character; hence in this model mixed types may be represented as superpositions of edge and screw dislocations. However, the line vector of each screw is independent of the slip plain, meaning that there are only 18 independent dislocation systems (12 edge and six screw). Thus the slip plane of the screw dislocations is left ambiguous, as in Evers, et al [52]. Because the simulated dislocation structures are random and the critically resolved shear stress of FCC slip systems are identical, all weight functions in Equation 1.11 were set to unity, which means that the total line length of dislocations (assumed to be proportional to total energy) is being minimized.

The simulated regions of interest were cubes with side length of 100 nm with the $(1\ 1\ 0)$ face of the crystal acting as the simulated sample surface. Kysar et al. suggest that the lower limit of measurable dislocation density should be much greater than $1/L^2$, where L is the step size of a scan (or in this case the side length of the simulated volume) [29]. This lower limit for

dislocation density corresponds to one dislocation passing through the volume (in the case of the current simulation, this value is $10^{14} m/m^3$); since this is the discrete case, it is somewhere below the lower limit of the continuum assumption.

For the initial test, only a single dislocation type with a density of $10^{15} m/m^3$ was simulated in each interaction volume. Measurable (via EBSD) distortion derivatives were calculated using the method described in Section 2.3 (the distortion was calculated at two points on the simulated surface, and the derivative taken numerically). This information was fed into each of the four implementations the Nye-Kroner method described in Section 3.1. These four methods differ in the number of constraints employed (3 or 6) and the starting point for the gradient based optimizer (the origin or the easily calculable least squares solution).

Dislocation fields of a single type are simulated for each slip system (eighteen trials in total). The distortions are calculated and fed into the Nye-Kroner method. The resultant dislocation field calculated by each method is given in Figure 3.1. Because the objective of this method is to identify the most prominent dislocation systems, the solutions were scaled to have the same magnitude as the simulations.

The Nye-Kroner method never completely matched the simulated dislocation densities for every simulation in any of its implementations (a perfect match would be indicated by the predicted dislocation density being identical to the simulated dislocation densities in the top-left on Figure 3.1). The Nye-Kroner method often predicts multiple types of dislocation density when in fact only one type is simulated. This occurs because multiple types of dislocation can contribute to the limited number of available strain / rotation gradient terms of the Nye tensor. Because some dislocations contribute more efficiently to certain Nye tensor terms, the local minimum often favors dislocation systems based on the orientation of the crystal.

On average, all of the methods over predicted the magnitude of the total dislocation density except for the 3-term implementation using the least squares solutions as a starting point. The average ratio of the predicted bulk dislocation density to the simulated was 1.4 and 1.5 for the 6-term method starting from the least squares solution and the origin respectively, while these numbers were 0.95 and 1.2 for the 3-term implementation. However, depending on the simulated dislocations orientation relative to the surface, these numbers could vary wildly.

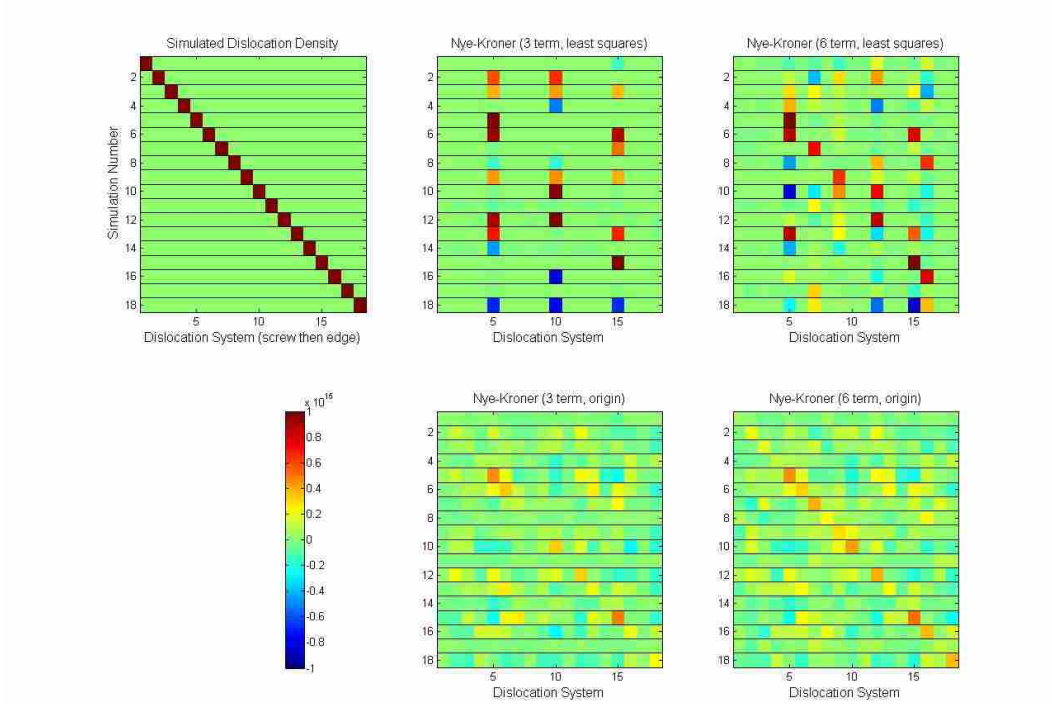

Figure 3.1: The simulated (top left) and predicted dislocation densities using the Nye-Kroner methods (the right four images) in m-2 for a single type of simulated dislocation density. The horizontal axis corresponds to the distinct slip system/line vector combination (6 screws followed by 12 edges). The vertical axis relates to the number of the simulation (i.e. each row represents a simulated volume element), and the color scale refers to the dislocation density assigned to each slip system.

The 6-constraint method predicted the simulated dislocation type as the most dominant one 15 times out of 18 when optimization began at the origin and 6 times when the least squares solution was used as a starting point. The 3-term method, on the other hand, only identified the correct dominant slip system 7 and 4 times. The fact that the 6-constraint method was able to resolve the correct type of dislocation more often suggests that the assumption that strain gradients are negligible compared to rotation gradients is at least somewhat valid.

As stated previously, when the Nye-Kroner method is implemented with a gradient based optimizer starting from the least squares solution, it can exactly predict simulated dislocation density if the dislocation type is oriented favorably to the surface. However, if the origin (i.e. all dislocation densities set to zero) is used as the starting point for the optimization algorithm, the algorithm is less likely to find the correct magnitude of dislocation density (typically low by a factor

of four), but more likely to identify the dominant dislocation density type (for this orientation, the 6 constraint method identified the correct dominant slip system eleven times out of 18).

For the rest of the demonstrations in this study, the Nye-Kroner method will be implemented using Pantleons six constraints, and a gradient optimizer starting from the origin, as this method has been shown in simulations to best be able to resolve dislocation density type, if not magnitude.

3.3 Demonstration in deformed single crystal nickel

In this section we validate the Nye-Kroner method on a real sample. In a recent paper, Kysar et al. examined the active dislocation systems of a nickel single crystal that underwent a carefully controlled plastic deformation process (wedge indentation) [29]. Because of the implications of plasticity around wedge indentations for fracture mechanics, this problem has been well studied [36, 48, 49]. By ensuring that the deformation was in-plane, Kysar, et. al. show that the components of the Nye tensor typically unavailable via EBSD are near zero; i.e. only the terms are significant, making the 3-constraint Nye-Kroner method ideal for this example. They demonstrated that only three effective slip systems could be activated, thus eliminating the need for the optimization implicit in Equation 1.11, and resulting in maps of relative activity on these systems.

Because of the extensive analysis of this highly constrained problem (including crystal plasticity validation [46,47], we consider Kysars results to provide an accurate baseline. The objective of this paper is to determine whether the Nye-Kroner approach for resolving GND activity onto individual slip systems, as described above (Equation 1.11), will arrive at similar results without making any assumptions about the deformation.

The sample was prepared by using a tungsten carbide indenter with a 90 included angle on the $(0\ 0\ 1)$ face of a nickel single crystal in the $[1\ 1\ 0]$ direction. The sample was then cut in half parallel to the $(1\ 1\ 0)$ plane to reveal the portion of the sample that experienced plane strain. The sample was then polished and a 0.15 mm $\times$ 0.15 mm area around the deformation was scanned using HR-EBSD to find the distortion gradients. The step size was 3 microns.

In the study cited above, it was shown that a line load applied parallel to the $[1\ 1\ 0]$ direction in an FCC crystal causes dislocation slip to occur on 3 effective slip systems of edge character, which are in fact combinations of two real edge dislocation systems [29]. Slip on these effective

systems accommodates plane strain loading. Each effective slip system is made up of two crystal dislocations (both edges) which have equivalent Schmid factor, and therefore should slip in equal proportion. These slip systems are delineated in Table 3.1.

These slip systems should theoretically be the dominant slip systems present in the sample. Dislocations present in the sample before deformation will be insignificant compared to the dislocations associated with deformation. Kysar et al. used EBSD data and a modified version of Equation 1.11 to map the dislocation density onto the effective systems; his approach used only the three effective dislocation types instead of all 18 unique crystallographic dislocation types, and assumed all the Nye tensor terms associated with out of plane deformation to be zero.

Using Kysars original EBSD data, the Nye-Kroner method (Equation 1.11) was implemented for this paper with all 18 unique dislocation types on the right hand side of the equation, and no assumptions about deformation. Gradient optimization was used with the origin as the starting point to solve the minimization problem in Equation 1.11. The tolerances on the constraints were relaxed to allow for noise of magnitude, /L, where L is the step size of the EBSD scan and is the estimated error of the HREBSD technique, which Wilkinson quotes as being on the order of 10^{-4} [12]. Dislocation density on each dislocation system was calculated. The dislocation density on the effective slip systems defined by Kysar were calculated by simply summing the dislocation density on each of the dislocation systems that make up the effective dislocations in order to directly compare with the previous studys results. The results are shown in Figures 3.3-3.3.

Dislocations associated with the effective slip systems were dominant, and effective slip systems 1 and 3 were antisymmetric to each other about the indenter tip (slip system one dominant to the right of the indenter and system 3 to the left), while effective slip system 2 is symmetric about it. All other dislocation systems have values below the noise level.

Table 3.1: Effective slip systems required to accommodate plane strain in the $(1\ 1\ 0)$ plane of an FCC crystal (see [29]).

Effective slip system	**Component crystallographic dislocation types (edges)**
1	$(1\ \bar{1}\ 1)[\bar{1}\ 0\ 1], (1\ \bar{1}\ 1)[0\ 1\ 1]$
2	$(1\ 1\ 1)[\bar{1}\ 1\ 0], (1\ 1\ \bar{1})[\bar{1}\ 1\ 0]$
3	$(\bar{1}\ 1\ 1)[1\ 0\ 1], (\bar{1}\ 1\ 1)[0\ \bar{1}\ 1]$

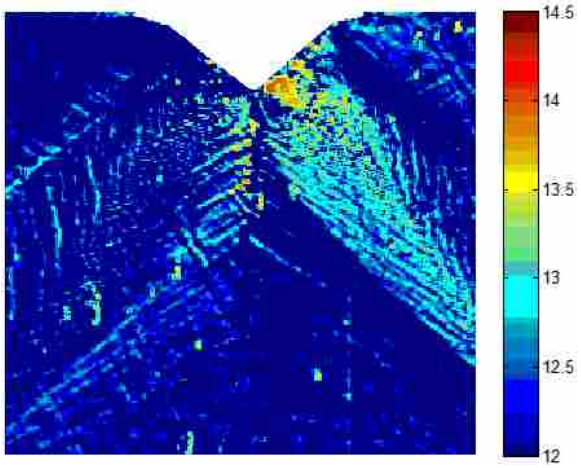

(a)

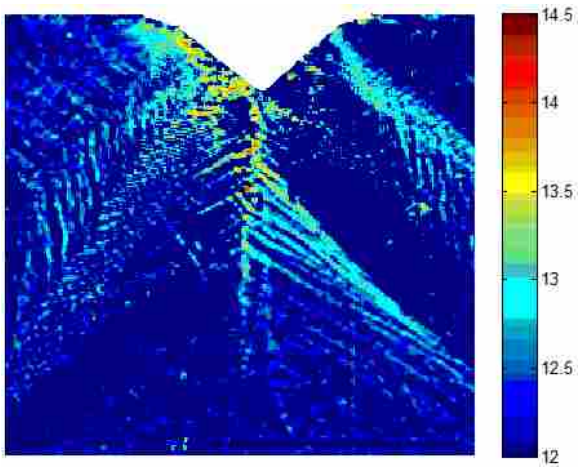

(b)

Figure 3.2: The positive (a) and negative (b) dislocation density on effective slip system 1, the $(1\ \bar{1}\ 1)[\bar{1}\ 0\ 1]$ and $(1\ \bar{1}\ 1)[0\ 1\ 1]$ edge dislocations, around an indented nickel single crystal as determined by the Nye-Kroner method. The scanned area is 0.15×0.15 mm. The color scale is in log units of dislocation density (m/m^3).

The results correspond well with Kysars results, but the general method presented here has the advantage that it requires no prior knowledge of the deformation of the sample. In the previous study, the median value of dislocation density was on the order of $10^{13} m/m^3$, as it is in this study. Thus, a general application of the Nye-Kroner method is just as effective at identifying both magnitude and type of dislocations due to planar deformation as a highly constrained method, as has already been suggested by simulation.

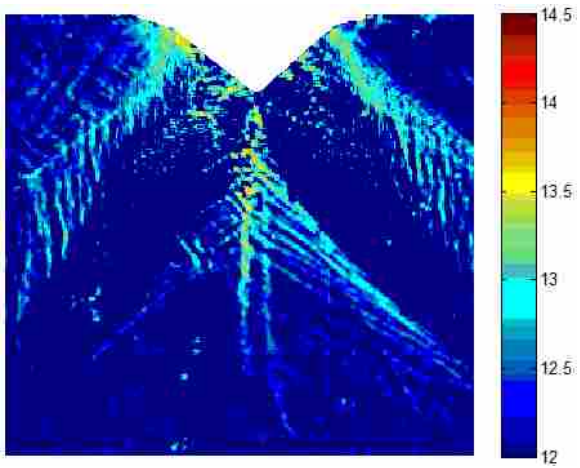

(a)

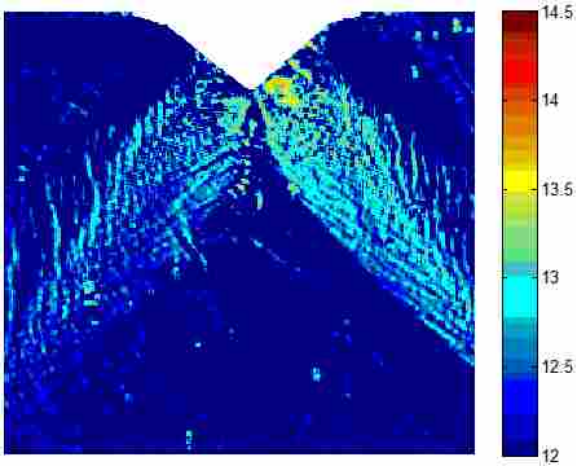

(b)

Figure 3.3: The positive (a) and negative (b) dislocation density on effective slip system 2, the $(1\ 1\ 1)[\bar{1}\ 1\ 0]$ and $(1\ 1\ \bar{1})[\bar{1}\ 1\ 0]$ edge dislocations, around an indented nickel single crystal as determined by the Nye-Kroner method. The scanned area is 0.15×0.15 mm. The color scale is in log units of dislocation density (m/m^3).

3.4 Conclusions

Multiple implementations of a Nye-Kroner type method for resolving dislocation densities onto individual slip systems were applied to simulations of dislocation density fields based on classical lattice mechanics. All of these implementations used gradient based optimization of total line length of dislocations, and differed only in the number of constraints employed and the starting point of the optimization algorithm. Adding the three additional constraints suggested by Pantleon

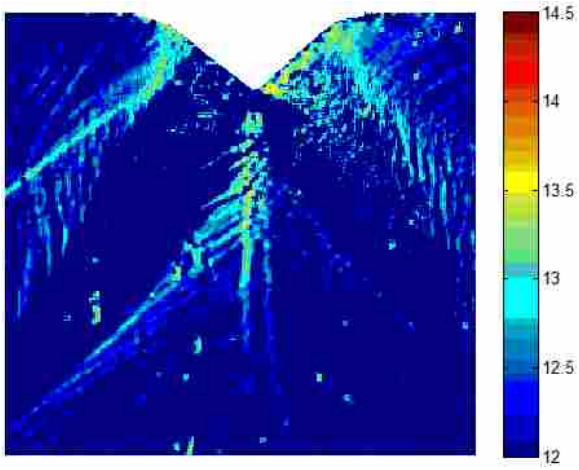

(a)

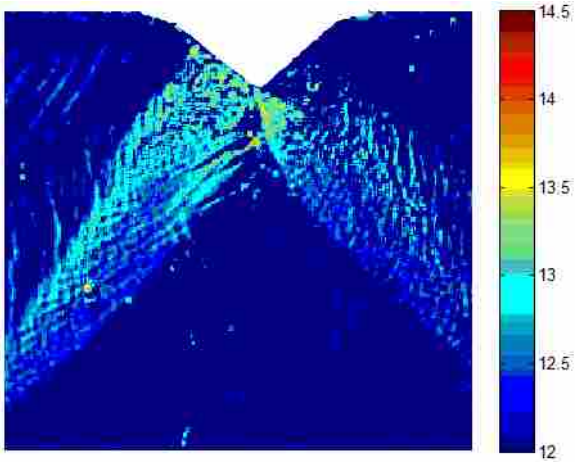

(b)

Figure 3.4: The positive (a) and negative (b) dislocation density on effective slip system 3, the $(\bar{1}\ 1\ 1)[1\ 0\ 1]$ and $(\bar{1}\ 1\ 1)[0\ \bar{1}\ 1]$ edge dislocations, around an indented nickel single crystal as determined by the Nye-Kroner method. The scanned area is 0.15×0.15 mm. The color scale is in log units of dislocation density (m/m^3).

allowed the Nye-Kroner method to correctly identify the dominant dislocation system 15 times out of 18, as opposed to only 7 for the 3 term implementation.

It was also found that the optimization algorithm is very sensitive to the starting point due to the small number of constraints (3 or 6) compared to the size of the search space (18 variables). Selecting the origin as the starting point was most effective at identifying dislocation type, whereas starting at the least squares solution was best at calculating the correct magnitude of dislocation density.

A previously analyzed dislocation field in wedge-indented single crystal nickel from a study by Kysar, et al. was used to demonstrate the application of the methods. The Nye-Kroner method as implemented here closely matched the previous study which was validated by an analysis of the deformation mechanics.

However, the Nye-Kroner method, even when optimized as in this chapter, still has a number of drawbacks. It is unable to accurately resolve magnitude and type. It also preferentially detects dislocations associated with plane strain deformation, due to the 2D nature of EBSD. The next chapter addresses these issues through the implementation of a novel method of relating lattice distortion information tot he dislocation content of a material.

CHAPTER 4. A NOVEL APPROACH TO RESOLVING DISLOCATION DENSITY ONTO INDIVIDUAL DISLOCATION SYSTEMS BASED ON CLASSICAL DISLOCATION MECHANICS

In Chapter 2 the difficulty in dealing with the minimization problem in the standard equation for EBSD CDM (Equation 1.11 was bypassed entirely by using a norm of the Nye tensor itself to estimate the total dislocation density. In Chapter 3 it was demonstrated that by carefully manipulating the optimization problem in the CDM equation, the geometrically necessary dislocation density on each dislocation system may be recovered adequately, particularly in the case of in plane deformation. However, The 6 constraints available from 2D Nye-Kroner methods are ultimately inadequate when attempting to recover dislocation density associated with arbitrary, out of plane deformation.

This chapter seeks to address the under constrained problem by bypassing the intermediary of the Nye tensor entirely, and instead relating dislocation content directly to the measured lattice distortion derivations. The framework applies the distortion field simulations from Section 2.2 for calculating local distortion in the region of a dislocation field, and compares these simulated distortions with the measured distortions, directly determined from HREBSD, to infer the contribution to GND content from different slip systems. The method relies on classical equations for the distortion around a single, discreet dislocation adapted for the continuum level by smearing over a region of interested. The result is a simple, numerically efficient, and effective relationship between dislocation content and the measurable lattice distortion.

In order to assess the performance of the lattice distortion framework, it is compared to more traditional approaches that utilize the Nye tensor. However, there is no single typical application of a Nye tensor-based method of relative activity determination. This Chapter will compare the new distortion matching technique to the four implementation of the Nye-Kroner method employed in Chapter 3. In the case of simulated dislocation fields the new distortion matching method

out-performs the Nye-Kroner method in all cases (including the more sophisticated implementation of Nye-Kroner).

4.1 The distortion matching method

In Section 2.2, a novel method of simulating distortion fields associated with dislocation density fields was presented. In Chapters 2 and 3, these simulations were used to evaluate current methods of relating measurable lattice data to dislocation density. In this chapter, however, we will use the simulations themselves to relate EBSD lattice distortion derivative data to the dislocation content of the material. We refer to the technique described in this section as the distortion matching method.

The distortion matching method takes the available slip systems for that particular material and lattice orientation, and assumes that slip occurs either by edge or screw dislocation formation / motion (i.e. that mixed dislocation can be written as a combination of these). The distortion gradient, $\beta^{*t}_{ij,k}$ (where the k index represents the direction of the derivative and the t superscript represents the dislocation system), caused by unit dislocation density is calculated for each type (using the analytical formulation presented above), and these are superimposed to determine the distortion associated with an assumed test dislocation field. The constraint that is applied in the search for the correct dislocation field is that the measured distortion gradient ($\beta_{ij,k}$ from HREBSD) must be compatible with the calculated distortion gradient for the assumed dislocation field.

Twelve lattice distortion derivative terms are available from surface HREBSD (see Equation 2.3). Because this number is generally lower than the number of dislocation types, the problem of resolving individual dislocation densities is still underconstrained. Nevertheless, the number of available constraints is significantly higher than for the Nye-Kroner method (Equation 1.11). Consequently, optimization must be employed to find a set of dislocation densities on each slip system that accommodates measured lattice distortion. The objective is to minimize the overall bulk dislocation density, assuming that nature will employ as little energy as possible to achieve an arbitrary deformation. A similar assumption is made in the Taylor method [53]. If more information is available concerning the relative CRSS of individual slip systems and/or Schmid factors, a weight function may also be introduced. Put succinctly, the distortion matching method for determination

of relative dislocation activity is as follows:

$$\text{minimize} \sum_{t=1}^{N} |w^t \rho^t|, \text{ s.t. } \beta_{\mathbf{ij},\mathbf{k}} = \sum_{t=1}^{N} \rho^t \beta^{*\mathbf{t}}_{\mathbf{ij},\mathbf{k}} \tag{4.1}$$

where w^t is the weight function, ρ^t is the dislocation density of an individual dislocation type, is the lattice distortion measured via HREBSD, and β^* is the lattice distortion resulting from a unit dislocation density of a particular type in the region of interest, as determined in the previous section. This equation effectively replaces Equation 1.11 in our formulation for CDM.

Clearly the twelve available distortion gradient terms may be separated into six strain terms and six rotation terms simply by separating the symmetric and antisymmetric parts. If the strain is neglected, there are only six constraints all associated with rotation which should be functionally equivalent to the six constraints Pantleon describes for traditional surface EBSD dislocation techniques [38].

For an FCC material Equation 4.1 represents an optimization problem with 12 linear constraints and 18 unknowns. Because of the absolute value operator in the objective function, there are a number of local minima. Hence gradient based methods should be used with care; several different starting points should be used for the optimization algorithm in order to check the validity of the final minimum. Generally, replacing the objective function in Equation 4.1 with the L_2 norm (which results in an easy to compute solution) proved to provide the best starting point for the L_1 norm search (i.e. most likely to result in a global minimum solution); this is the method employed in this paper. However, this method was relatively insensitive to the starting point as compared to the Nye-Kroner method.

4.2 Validation of the distortion matching method via simulation

In order to validate the proposed method and compare it with the Nye-Kroner approach, simulated volume elements were generated with known dislocation content. Nickel was selected as the simulated material. As an FCC material, it has 12 slip systems, each of which may be of edge or screw character (in reality, nearly all dislocations are of mixed character, but in this model they must be represented as superpositions of edge and screw dislocations). However, the distortion fields of the screw dislocations are independent of the slip plane and depend only on the

Burgers vector. This means that to the algorithm, each screw is identical to a second screw with the same Burgers vector. To improve efficiency, the number of screws is reduced to 6 instead of 12 where the slip plane of the screw dislocations is left ambiguous as in Evers, et al [52]. Because the simulated dislocation structures are random and the CRSS of FCC slip systems are identical, all weight functions in Equations 1.11 and 4.1 were set to unity.

The simulated regions of interest were cubes with side length of 100 nm with the $(1\ 1\ 0)$ face of the crystal acting as the simulated sample surface. Kysar et al. suggest that the lower limit of measurable dislocation density should be much greater than $1/L^2$, where L is the step size of a scan (or in this case the side length of the simulated volume) [29]. This lower bound dislocation density (in the case of the current simulation, $10^{14} m/m^3$) corresponds to one dislocation passing through the volume, and represents an absolute lower limit below the continuum assumption.

For the initial test, only a single dislocation type with a density of $10^{15} m/m^3$ was simulated in each interaction volume. Measurable (i.e. surface) distortion derivatives were calculated using the method above (the distortion was calculated at two points on the simulated surface, and the derivative taken numerically). This information was fed into the distortion matching method explained above (Equation 4.1) to find the physically most probable set of dislocation densities that matched the constraints and minimized total slip.

Next, the Nye-Kroner method (Equation 1.11) was applied to the same simulations. In practice there are many variations to this method depending upon the number of Nye tensor components that are used in the constraints, the weights employed, and the optimization approach. Most approaches ignore the strain components of the Nye tensor (see Equation 2.3), as explained above. However, simulations of distortion from test fields indicate that the strain gradients are of similar magnitude to the rotation gradients in Equation 2.3. The simulations may not accurately match real discrete fields, where the strain fields may drop off rapidly near the dislocation, and hence not additively combine as they do in the simulations, but the simulations do match Greens function methods, as mentioned previously. On the other hand, real data from some materials indicates non-negligible strain components for several trials undertaken by the authors; this area of analysis needs further investigation. If the strain components are included in the analysis, only three terms of the Nye tensor can be unambiguously recovered using HREBSD the (α_{i3}) terms. If the strain terms are neglected, further terms are available.

Hence we adopt two approaches to the Nye-Kroner method for the purposes of comparison with the distortion matching method. The first (the 3-constraint method) uses the full set of (α_{i3}) terms (i.e. including the strain components, hence resulting in higher accuracy than a typical implementation by previous authors). The second uses the six constraints suggested by Pantleon [38]. In addition to the α_{i3} terms, α_{12}, α_{21} and the difference (α_{11} α_{22}) are available for inclusion in Equation 1.11. For the assumed FCC material, Equation 1.11 represents an optimization problem with the 3 or 6 linear constraints and 18 unknowns. On the surface, Equation 1.11 appears to be a simple linear programming problem, i.e. the objective function and constraints are all linear. Linear programming problems are convenient because the Kuhn-Tucker [50] conditions may be used to solve directly for the optimum. However, the discontinuities associated with the absolute value function mean that there are a large number of potential minima ($2N$, where N is the number of dislocation types), making direct calculation impractical and gradient based optimization problematic because of high sensitivity to initial position.

To circumvent this problem, multiple approaches were examined. The first approach utilizes different starting points with gradient based optimization. Of the available starting points, two were selected as representative: the L_2 norm (least squares) solution (which may be easily calculated), and the point where all dislocation densities were zero (the origin). Besides a gradient based method, a stochastic optimization algorithm was also employed, namely particle swarm optimization [51]. However, using gradient based methods with the least squares solution as the starting point proved to reach the global optimum very consistently, obviating the need for computationally expensive stochastic optimization.

In considering the choice of starting point, something interesting was observed. When the algorithm is applied using the L_2 norm starting point, and the global optimum is reached, the Nye-Kroner method can sometimes precisely predict both the magnitude and type of dislocation content; but if the dislocations are not oriented favorably, Nye-Kroner completely misses the dislocation content or mistakes the dislocation type. However, when the origin is used as the starting point, the local optimum that the algorithm comes to tends to predict the correct dislocation type more frequently, albeit at the wrong magnitude and with noise on the other dislocation types.

For the purposes of comparison with the distortion matching method the Nye-Kroner method is implemented in four ways, using 3 and 6 constraints and using the origin or the least squares

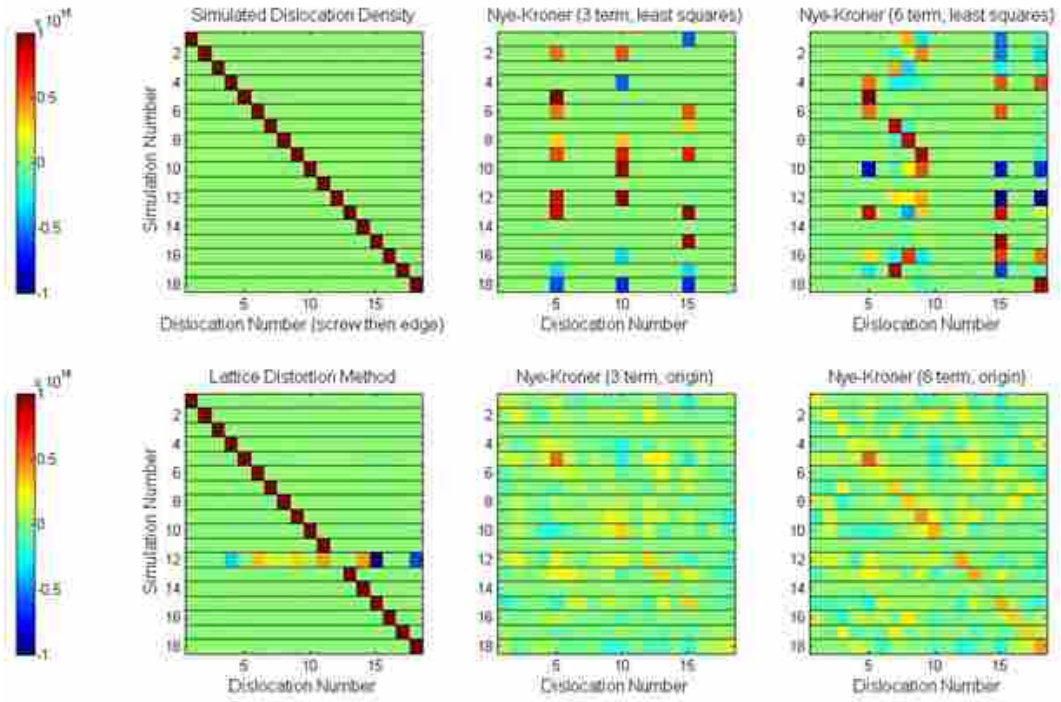

Figure 4.1: The simulated (top left) and predicted dislocation densities using both the distortion matching method (bottom left) and the Nye-Kroner methods (the right four images) in m/m^3 for a single type of simulated dislocation. The horizontal axis corresponds to the distinct slip system/line vector combination (12 edges followed by 6 screws). The vertical axis relates to the number of the simulation (i.e. each row represents a simulated volume element), and the color scale refers to the dislocation density assigned to each slip system.

solution as the starting point for the gradient based optimization algorithm. These methods are explained in more detail and validated in Chapter 3. For the first test, dislocation fields of a single type are simulated for each slip system (eighteen trials in total). The distortions are calculated and fed into the Nye-Kroner method and the distortion matching method. The resultant dislocation field calculated by each method is given in Figure 4.1.

Clearly, with only a single type of dislocation present, the added constraints of the distortion matching method allow for a more accurate recovery of the relative activity of each slip system, leading to virtually zero error in all but one case. The Nye-Kroner method, on the other hand, was not as successful, never completely matching the simulated dislocation densities in any of its implementations.

The Nye-Kroner method will often predict multiple types of dislocation density when in fact only one type is simulated. This occurs because multiple types of dislocation can contribute

to the limited number of available strain / rotation gradient terms of the Nye tensor. Because some dislocations contribute more efficiently to certain terms, the local minimum often predicts smaller dislocation densities on several different slip system combinations. The distortion matching method sometimes suffers from similar ambiguity, but because of its additional constraints, it can more accurately resolve individual types of dislocation density.

The complexity of dislocation structure (i.e. how many different dislocation systems there are) has a strong influence on the ability of the algorithm to find the ideal solution, so matching the complexity of real materials was important to validate these methods. The Taylor model suggests that at least five independent slip systems are required to accommodate arbitrary strains. Hence, dislocation fields with up to six distinct dislocation types were simulated. Eighteen random networks of dislocations with dislocation densities in a suitable range were simulated and the performance of the distortion matching method and the most successful Nye-Kroner implementation were compared. The results are presented in Figure 4.2.

By comparing the simulated and calculated dislocation content on the top row of Fig. 2, the distortion matching method is clearly superior to the Nye-Kroner method. This is emphasized further by consideration of the error for each dislocation type, for each simulation, plotted on the bottom row. The distortion method results in a much lower error across all of the simulations undertaken.

On average the distortion matching method captured 99% of the bulk magnitude of the simulated dislocation density, whereas the Nye-Kroner method only captured 86%. If the solution vector in 18-dimensional space is compared to the simulated dislocations, the distortion matching method is accurate, on average, to within 6 degrees and the Nye-Kroner method is only accurate to about 57 degrees. Furthermore, the accuracy of the distortion matching method would be even greater were it not for one poor simulation (simulation 1).

The Nye-Kroner results demonstrate markedly more error whether simple or complex dislocation structures are considered. The algorithm tends to successfully identify certain dislocations more readily due to their favorable orientation relative to the surface. In general, if only the bulk dislocation density is required, these simulations suggest that the Nye-Kroner method does calculate dislocation densities in the right order of magnitude, but does not accurately recover the relative activity of each system.

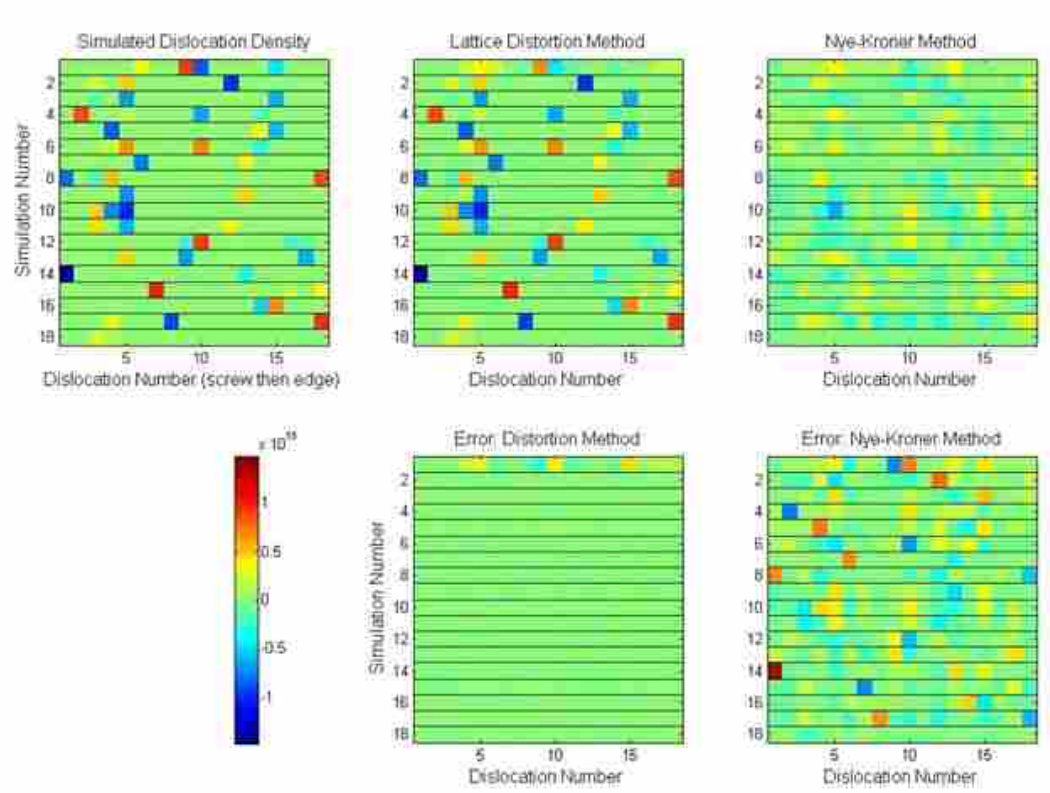

Figure 4.2: The simulated and predicted dislocation densities using both the distortion matching method and the Nye-Kroner method (top row) in m/m^3 for a random dislocation network. Also plotted is the error (the difference between the simulated and measured dislocation densities) of each method (bottom two images). The vertical axis relates to the number of the simulation, whereas the horizontal axis relates to the dislocation type present in the simulated interaction volume.

4.3 Conclusions

A new framework has been proposed for determining relative activity of GND content using all available distortion components from HREBSD, and comparing calculated distortion from test fields with the measured values. The calculated distortion uses classical lattice distortion fields around dislocations, adopted for a continuum view, the same simulations used to validate the methods presented in previous chapters. In simulations of simple (consisting of only one dislocation type) and complex (multiple dislocation types) dislocation fields, the distortion matching method had enough information to resolve dislocation content precisely with little error. The large number of linear constraints available (12) compared to the number of variables (18 for FCC crystals)

reduced the size of the search space and made optimization simple and relatively independent of starting point.

Multiple implementations of the more traditional Nye-Kroner method of dislocation content resolution were also applied to these simulations, as is more fully explained in Chapter 3. Applying the three most commonly used constraints in Equation 1.11 (based upon the terms α_{i3}, with the addition of strain terms available from HREBSD) the Nye-Kroner method performed significantly worse than the lattice distortion approach. Adding three additional constraints [38] improved the ability of the algorithm to resolve dislocation content somewhat, despite the fact that these three constraints rely on the assumption that the strain gradients are negligible compared to rotation gradients (they are in fact of the same order of magnitude). It was also found that the optimization algorithm is very sensitive to the starting point due to the small number of constraints (3 or 6) compared to the size of the search space (18 variables). Selecting the origin as the starting point was most effective at identifying dislocation type, whereas starting at the least squares solution was best at calculating the correct magnitude of dislocation density.

The Nye-Kroner method particularly struggled when multiple dislocation types were simulated. The distortion matching method (Equation 4.1) was superior at resolving dislocation content onto individual slip systems compared to implementation of any of the possible Nye-Kroner approaches (Equation 1.11) for simulated fields. The distortion matching method precisely measured the dislocation density for 17 of the 18 simulated dislocation types, whereas the Nye-Kroner method identified the dominant dislocation type only 11 times out of 18, and was off on average by a factor of four for the magnitude of that dislocation type.

Simulations suggest that the distortion matching method presented in this paper can better resolve dislocation content (particularly dislocation content associated with out of plane deformation), than the conventional Nye-Kroner method because it incorporates more of the information available from developing high resolution EBSD techniques into constraints. This would allow EBSD dislocation microscopy to characterize arbitrary deformation without employing three dimensional techniques.

CHAPTER 5. THE EFFECT OF LENGTH SCALE ON THE MEASUREMENT OF GEOMETRICALLY NECESSARY DISLOCATIONS VIA EBSD CONTINUUM DISLOCATION MICROSCOPY

CDM typically approximates local gradients from a grid of discrete measurement points. The spacing of this raster, which we denote as L, not only determines the numerical accuracy of the gradient determination, but it defines the implicit Burgers vector. This paper investigates the effect of this grid length scale (or step size) on measurements of GND density via EBSD CDM. Researchers have already shown that measured dislocation density is a function of the step size between neighboring points of the EBSD scan [54–56]. Measured lattice distortion gradients are highly sensitive to both real lattice fluctuations and noise of various kinds when taken over a range of step sizes. Thus efforts have focused on selecting a single optimal step size, or a range of safe step sizes, that are long enough so that noise effects do not dominate, and short enough to resolve important deformation features [29]. However, reporting GND density for a single step size may not always be appropriate; some physical information may be better obtained by analyzing measured GND content at a number of different length scales.

At low step sizes, the measured GND density is proportional to the inverse of the step size of the lattice distortion numerical derivatives [54]. This low step-size relationship results from an approximately constant measured distortion between points in the raster independent of step size between the points of interest. Two phenomena have been proposed to explain this, algorithmic noise in the relative distortion determination and the transition of statistically stored dislocations (SSDs) to GNDs. Previous work suggests that algorithmic noise is much less significant than the effect of the SSD to GND transition [56].

GNDs are dislocations that are associated with long range distortion gradients in material, relating to heterogeneous deformation [3]. SSDs, in contrast, have no long range geometric effect because their distortion fields are cancelled by other dislocations, and they are associated with homogeneous deformation. There is no physical difference between SSDs and GNDs; they are

only distinguished by their distribution. This may be understood by imagining a large Burgers circuit. All dislocations within the circuit whose distortion effects are not canceled by other dislocations are GNDs; these dislocations contribute to distortion gradients above the length scale of the Burgers circuit. Dislocations within the circuit that collectively cancel each others distortion fields (effectively dislocation dipoles) are SSDs. If the circuit contains a single dislocation (e.g. at the TEM length scale), then the dislocation is a GND at that length scale. If a larger size of Burgers circuit is chosen, more dislocations within the circuit will match with dislocations of opposite sign, forming dislocation dipoles with not net geometric effect; these dislocations are now SSDs. Hence the distinction between SSDs and GNDs is length scale dependent. For EBSD, the size of the implicit Burgers circuit is related to the step size. Thus, the measured GND density will depend on the step size used.

For a fairly homogeneous distribution of dislocations, the cancellation of distortion effects as more dislocations are included in a growing Burgers circuit explains the $1/L$ dependence reported by other authors. However it is well documented that plastic deformation typically leads to heterogeneous distributions of dislocations at some length scale - either due to pile-up at grain boundaries or to dislocation substructure (cells, cell blocks, geometrically necessary boundaries, etc [57, 58] or due to heterogeneous deformation [36]. At the length scales of the heterogeneity, strain gradients are present. These dislocations associated with strain gradients may be thought of as true GNDs. Since these are real gradients, measurement of these true GNDs is relatively insensitive to the step size used to quantify them. As the step size increases, the effects of homogeneously distributed dislocations will become insignificant (due to the nature of the 1/L relationship) compared to the effect of heterogeneously distributed dislocations (true GNDs). Hence a graph of dislocation density versus step size shows a transition from the 1/L relationship to an almost constant GND density at moderately high step sizes (the exact threshold will depend on the relative amount of homogeneously distributed and heterogeneously distributed dislocations). This behavior has not been reported in literature; data supporting it will be presented here. These non-canceling true GNDs have also been incorporated into the statistical model of SSD to GND transition.

Once the measurement step size is greater than the characteristic length scale of the heterogeneously distributed dislocations, the level of detected GND density drops off as the step size is too large to resolve the substructure of the material. Additionally, for extremely large grains or

single crystals, crystal symmetry can limit the measurable lattice distortion. Many HREBSD algorithms have a simple misorientation cutoff to avoid error due to avoid comparing patterns between different grains or subgrains. All of these effects lead to a drop-off in measured dislocation density at very high step sizes. This drop-off in the GND-step size relationship may also be modeled statistically to determine an upper bound to step size.

The purpose of this chapter is to:

- Model the relationship between measured GND content, total dislocation content, true GND content, and interrogated length scale using basic statistics;
- Validate this model on a number of different samples;
- Use this model to provide criteria for EBSD step size selection;
- And use this statistical model to extract additional information about the total dislocation content of the material.

5.1 Methods and materials

In order to examine to step-size dislocation density curve over a large range of step sizes, large grained or single crystal samples are preferred. For this study, a tantalum single crystal prepared by collaborators at Columbia University was used. The sample was deformed with a 90 degree micro-indenter, sectioned and polished so that most of the strain lies in the plane of the EBSD scan. This is the same sample used in Chapter 2.

The sample was scanned over a much smaller area near the indenter tip to ensure a high amount of heterogeneous deformation, associated with GNDs and strain gradients. The scan was 10×10 microns with a step size of 20 nm. Dislocation density was calculated at each point using Equation 2.2. Because it is impractical to conduct a large number of scans at various step sizes, the scans were post processed multiple times, increasing the step size by skipping points in the raster. The microscope details are the same as in Chapter 2.

In addition to the tantalum single crystal described, this paper will investigate the dislocation density versus step size behavior for a number of engineering materials cursorily, as well, to show that the observations made in the paper are broadly applicable. This additional data comes

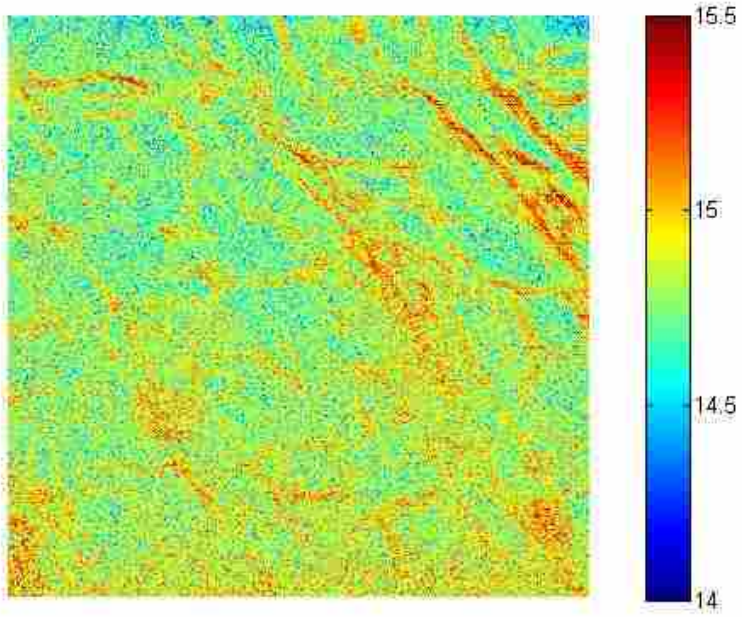

Figure 5.1: The dislocation density map for a 10×10 micron area beneath the indenter for a Ta single crystal deformed by micro indentation. The dislocation density is presented in log units of m/m^3. This sample was originally studied in [15].

from a number of studies conducted in our research group. For brevity, the sample preparation information and scan parameters of these scans is not provided here.

5.2 Results

The dislocation density of the Ta sample described in the previous section at the lowest step size is shown in Figure 5.1. The average measured GND density at various step sizes for the indented Ta crystal is shown in Figure 5.2. The dislocation density is averaged for a large number of points from a scan to show the trend in the data. There is a complex relationship between the step size of an EBSD scan (L in Eq. 1.10) and the measured dislocation density (ρ in Eq. 2.2). If we think of this relationship as a curve for visualization purposes, we note three distinct regions of the curve at various length scales, only one of which has been strongly represented in literature so far. An example of this curve is shown in Figure 5.2. Note that three distinct regions (labeled A, B

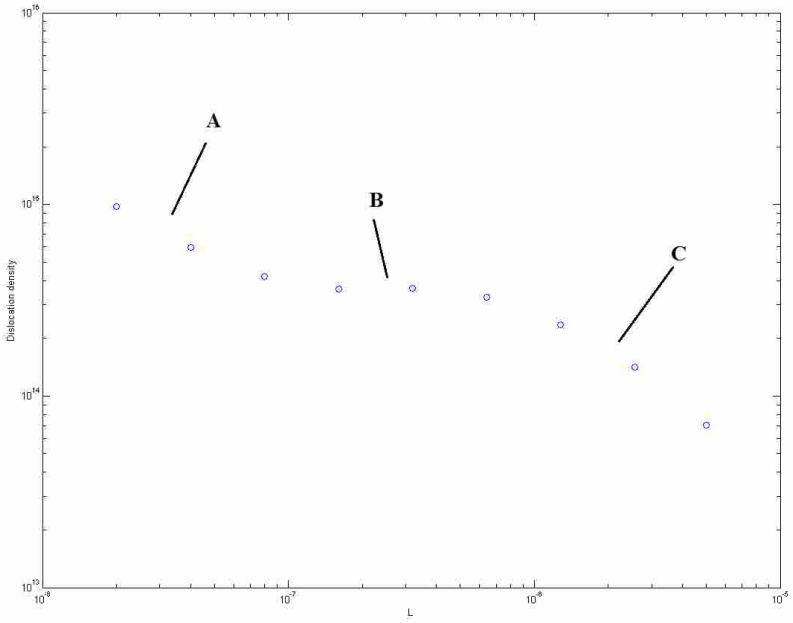

Figure 5.2: The average measured GND density versus step size curve of a micro-indented single crystal of tantalum near the indenter tip. Note that the (A) low step size $1/L$ relationship, the (B) relatively constant GND density region at moderate step size, and the (C) large step size drop off are all visible. Most scans will not show all three regions. This sample was originally studied in [15].

and C) of this curve are evident. The mechanisms behind these three regions were discussed in the introduction, and they will be explained more thoroughly here.

The first region of the curve is the one best characterized in the literature; Field and Jiang have both reported this inverse behavior [54, 56]. At low step sizes, measured GND density is inversely proportional to step size. As mentioned above, this relationship is attributed to some combination of algorithmic noise and/or the SSD to GND transition. In the Ta sample, this region is almost entirely absent because of the large amount of GNDs. To show that the inverse step size relationship is near universal at small step sizes, EBSD scans from a number of different annealed materials were examined. Measured GND versus step size curves for annealed magnesium, copper, and iron as well as epitaxial germanium at low step sizes are shown in Figure 5.3. Note that all of them roughly follow a $1/L$ type relationship, region A from Figure 5.2.

There is a certain amount of noise in determining the relative distortion between two EBSD patterns using HREBSD associated with limited resolution of the phosphor screen, as mentioned in

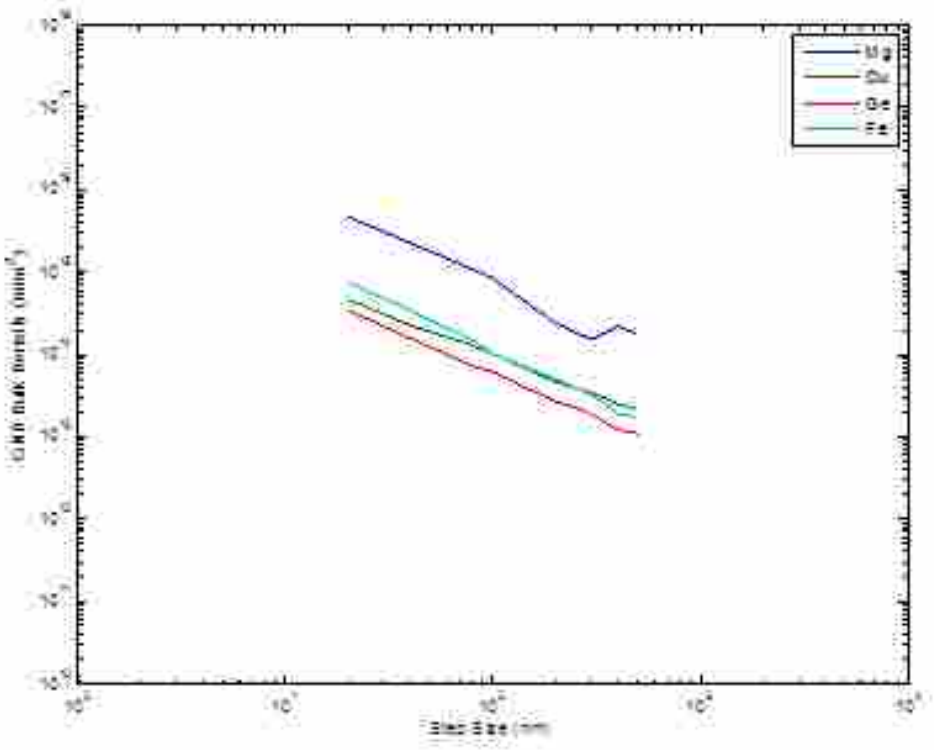

Figure 5.3: Measured GND curves for annealed magnesium, copper, and iron as well as epitaxial germanium at low step sizes. For comparison, the postulated resolution limit due to the inherent noise in HREBSD is also plotted.

the background section. Low quality patterns will also contribute to noise in the cross-correlations, but generally it is assumed for high quality scans that phosphor screen resolution error will be more significant. Wilkinson provides a rough estimate of the error in distortion calculation due to phosphor screen resolution at around 500 microstrain [12] (Compare this to the 0.5 degree accuracy of conventional EBSD [59–61], which corresponds to almost 9000 microstrain [23]). When Jiang investigates this lower bound using an epitaxially grown Si sample, he detects error about an order of magnitude higher [56].

The error in distortion calculation is random with a relatively constant average, but when the numerical derivative of lattice distortion is calculated, the relative distortion is divided by the step size which could lead to the 1/L relationship frequently observed (see Equation 1.10). However, Jiang points out that this level of noise is still orders of magnitude lower than the measured dislocation density, suggesting SSD to GND transition is the dominant effect on the measured GND density/step size relationship. The fact that this portion of the curve has been shown to increase

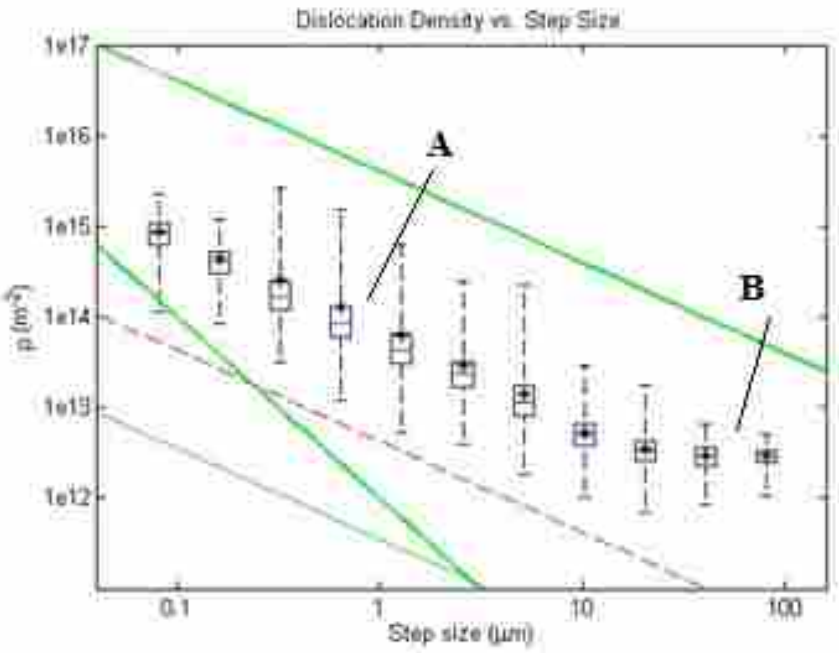

Figure 5.4: Measured GND density curve for deformed iron. Note that at higher step sizes the curve levels off into a relatively constant region.

in magnitude in response to deformation further supports the idea that GND to SSD transition is responsible for the inverse step size region [56].

At larger, moderate step sizes the $1/L$ relationship gives way to a region where the measured GND density is roughly constant, region B in Figures 5.2 and 5.4. We postulated in the introduction, it is suggested that this constant region is the result of true GNDs that accommodate strain gradients on the scale of the substructure of the material. What constitutes a low or moderate step size depends on the quantity and nature of the dislocation content of the material, and will be further explained in the next section. For comparison with the Ta sample, which had a high degree of heterogeneity associated with the deformation it underwent, the GND curve of a deformed piece of iron is shown in Figure 5.4. Note the significantly lower magnitude of the B region as compared to the Ta sample. This result supports the idea that the B region of a measured GND density versus step size curve is related to strain gradients caused by heterogeneous deformation.

Finally, at large step sizes (again, the transition between these various regions depends on the nature and quantity of deformation of the sample) the constant region gives way to yet another

$1/L$ type region. This drop off is only observed at very large step sizes, often larger than the grain size of most engineering materials, and thus is not frequently observed. This region of the curve is visible in the GND curve of a micro-indented single crystal of tantalum seen in Figure 5.2.

5.3 Modeling the GND density-step size relationship statistically

Now, we will model the various regions of the measured GND versus step size curve statistically. The GND to SSD transition seems to be the most likely explanation for the variation in measured GND density at different step sizes, both because the estimated noise of HREBSD is far lower than most measured dislocation densities and because the GND curve moves out in response to deformation, as discussed in the previous section. Modelling the curve as a function of the GND and SSD content of the material will allow the extraction of SSD information via EBSD, as well as provide criteria for step size selection.

Adams and Kacher attempted to model this transition with a simple 2D Monte Carlo simulation [62], which modeled dislocations all of a single type passing through a plane as points with either a positive or negative character. Dislocations of each sign were randomly distributed with more positive dislocations being simulated than negative so that there are net, geometrically necessary dislocations at every length scale. The net dislocation density is calculated inside of a number of boxes with varying side length by subtracting the included negative dislocations from the included positive dislocations,taking the absolute value, and dividing by the area of the box. This side length is analogous to the step size of the lattice distortion numerical derivative for a real scan. The average measured GND density from a large number of boxes can then be plotted versus the step size. The authors of the current paper duplicated this simulation, which is schematically illustrated in Figure 5.5. The simulated total dislocation density is $5.625 \times 10^{13} m/m^3$ and the density of unpaired true GNDs is $6.25 \times 10^{12} m/m^3$.

This curve may also be calculated analytically. For a randomly distributed field of positive dislocations with density ρ^+, the average number of dislocations in an $L \times L$ region will be represented by a Poisson distribution, which expresses the probability of a number of random events occurring in a region of space. The number of negative dislocations will also be characterized by a Poisson distribution. The expected value (the expected value of a Poisson distribution is also the

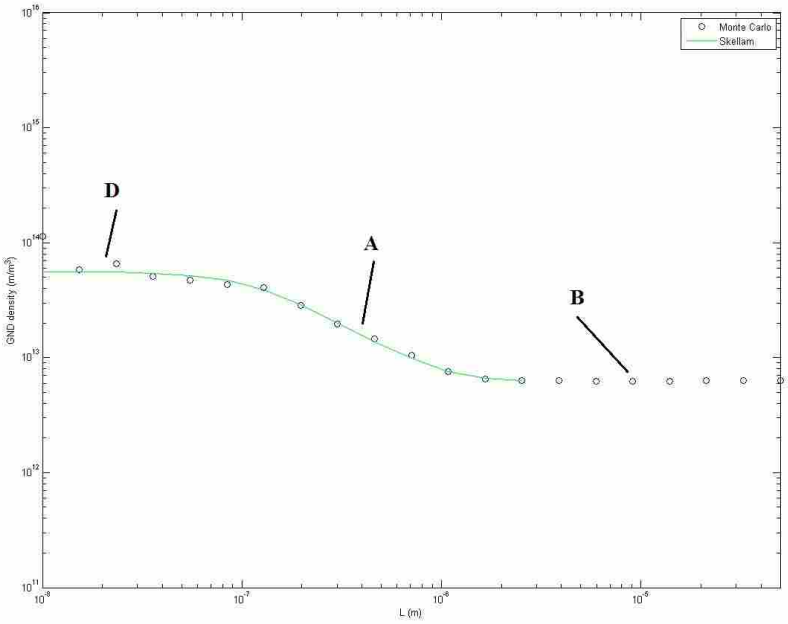

Figure 5.5: This figure shows a Monte Carlo simulation for a measured GND density versus step size curve as well as a Skellam model. The simulated total dislocation density is $5.625 \times 10^{13} m/m^3$ and the density of unpaired true GNDs is $6.25 \times 10^{12} m/m^3$.

variance) for each of these distributions is:

$$\lambda^+ = \rho^+ L^2 \tag{5.1}$$

$$\lambda^- = \rho^- L^2 \tag{5.2}$$

In order to understand the net dislocation density, we will need to take the difference between the number positive and the number of negative dislocations inside the square. The difference between two variables each having a Poisson distribution is a Skellam distribution. The Skellam distribution for the number of net dislocations is as follows:

$$P(k,L) = exp(\rho^+ L^2 + \rho^- L^2) \left(\frac{\rho^+}{\rho^-}\right)^{k/2} I_{|k|}(2\sqrt{\rho^+ \rho^- L^4}) \tag{5.3}$$

In this equation, $P(k,L)$ is the probability of k dislocations lying within an $L \times L$ square on the plane and I is the modified Bessel function of the first kind. Finally, the average measured dislocation

density may be calculated by taking the average of the absolute value of the difference and scaling by the box area as follows:

$$\bar{\rho}_m = \frac{\sum_{-\infty}^{\infty} |kP(k,L)|}{L^2} \tag{5.4}$$

Using Eq. 5.4 to calculate the expected measurement of GND density nearly perfectly fits the 2D Monte Carlo simulation (see Figure 5.5). At large step sizes the numerator of Equation 5.4 becomes too large to calculate using a double precision variable, and the result is not defined, which is why the Skellam model does not cover the whole range of the Monte Carlo simulation.

The Skellam model fit the Monte Carlo simulation perfectly, and the A and B regions from actual GND density versus step size curves are clearly visible (see Figures 5.2 and 5.4). However, the Skellam model and the Monte Carlo simulation have a constant region at very low step sizes (labeled D on Figure 5.5) the same magnitude as the total simulated dislocation density. The Skellam model also fails to accurately model the drop off (region C in Figure fig:tawedgecurve). Additionally, calculating points on the curve is computationally expensive and numerically unstable. The Skellam model is valuable because it is intuitive, but it is not practical to apply to real data because of these reasons. We will instead adapt this model to more accurately reflect real HREBSD CDM, which will lead to greater verisimilitude and well as improved computational efficiency.

At this point, it should be noted that EBSD dislocation microscopy does not work by counting discrete dislocations, rather by measuring continuous distortion derivatives. As such, the discreet nature of the simulation and the Poisson and Skellam distributions is perhaps not the best means of modelling the GND step size relationship at very low step sizes in real materials. Discreet counting is responsible for the flat region at low step sizes in the Monte Carlo simulations and the Skellam model seen in Figure 5.5. Instead, we modify our model by replacing the discreet Skellam distribution with the continuous Gaussian normal distribution closest to the Skellam distribution. We model the number of detectable dislocations of a certain sign inside of an $L \times L$ square as a normal distribution with mean and variance both equal to λ (which is approximately equivalent to the Poisson distribution for large λ). The difference between the number of positive and negative dislocations in the $L \times L$ square will also be a normally distributed variable with a mean of $\rho_{GND}L^2$ and a variance of $\rho_{total}L^2$, where $\rho_{GND} = \rho^+ - \rho^-$ and $\rho_{total} = \rho^+ + \rho^-$. The variable ρ_{GND} may be thought of as the true dislocation density discussed in the introduction. Making these

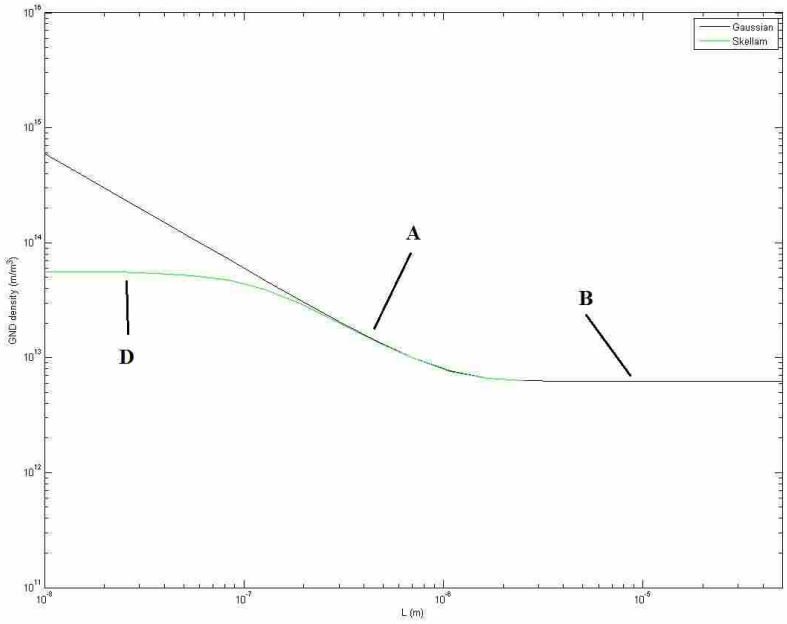

Figure 5.6: This figure shows the improved Gaussian model of a GND versus step size curve as well as the Skellam model. The dislocation density parameters are the same as Figure 5.5.

substitutions, the average measurable dislocation density may be calculated as:

$$\bar{\rho}_m = \frac{\int_{-\infty}^{\infty} |xf(x, \rho_{total}L^2, \rho_{GND}L^2)|dx}{L^2}$$
$$= \sqrt{\frac{2}{\pi}} exp\left(\frac{-\rho_{GND}^2 L^2}{2\rho_{total}}\right)\frac{\sqrt{\rho_{total}}}{L} + \rho_{GND} erf\left(\frac{\rho_{GND}L}{\sqrt{2\rho_{total}}}\right) \quad (5.5)$$

where $f(x, \sigma^2, \mu)$ is the Gaussian normal distribution probability density function and $erf(z)$ is the error function. Equation 5.5 has the advantage of being much more efficient to calculate than the Skellam model (Equation 5.4) due to the integrable nature of the Gaussian distribution.

This function is plotted in Figure 5.6 along with the Skellam model from Figure 5.5. Note that at high step sizes, this formulation (Eq. 5.5) is equivalent to the Skellam distribution fit (Eq. 5.4), but at lower step sizes where the Skellam-based curve and the simulation converge to total dislocation density, Eq. 5.5 remains a $1/L$ type relationship. The behavior of the Gaussian model better fits the behavior of real samples, as shown in Section 5.2.

Our improved model, which employs a Gaussian normal distribution instead of a Skellam distribution, now more accurately models real GND density versus step size curves like those seen in previous sections. However, it still does not model the drop off region of these curves (i.e. region C in Figure 5.2). This region of the measured GND density vs. step size relationship is typically only observed at step sizes larger than the grain size of most engineering materials,so this behavior is usually only seen in large-grained or single crystal samples.

This drop sometimes occurs due to crystal symmetry. This occurs because there is always some ambiguity when dealing with rotating crystals due to symmetry. HREBSD addresses this ambiguity by always assuming that two patterns are as close to each other in orientation space as possible. With real rotations that are quite large, HREBSD may measure a smaller misorientation associated with a different crystal symmetry. Because rotation is the most significant part of the measured distortion, and because measuring the rotation between two lattices far away from each other in orientation space will lead to smaller, erroneous rotation, crystal symmetry effectively caps the maximum measurable distortion between points. In other cases the drop may be due to dislocation substructure within the grain. If we imagine the dislocation substructure to be some pseudo periodic waveform, the numerical derivative will drop off when the step size exceeds the characteristic length scale of the structure.

However, it is typically not valuable to observe the dislocation density at length scales long enough that limitations due to crystal symmetry or dislocation subtructure become the limiting factor is distortion determination, as this recovered distortion would be erroneous. In order to prevent this, our algorithm checks the misorientation between patterns before determining the relative distortion, and simply throws out all derivatives associated with pattern misoriented from one another above a certain threshold, usually a few degrees. This effect may be simulated in the

model simply by modifying the bounds of integration in Eq. 5.5, as follows:

$$\begin{aligned}\bar{\rho}_m &= \frac{\int_{-qL}^{qL} |xf(x,\rho_{total}L^2,\rho_{GND}L^2)|dx}{L^2} \\ &= \frac{\sqrt{\rho_{total}}}{L\sqrt{2\pi}} \frac{2exp\left(\frac{-\rho_{GND}^2L^2}{2\rho_{total}}\right) - exp\left(\frac{-(q+\rho_{GND}L)^2}{2\rho_{total}}\right) - exp\left(\frac{-(q-\rho_{GND}L)^2}{2\rho_{total}}\right)}{\frac{1}{2}erf\left(\frac{q-\rho_{GND}L}{\sqrt{2\rho_{total}}}\right) + \frac{1}{2}erf\left(\frac{q+\rho_{GND}L}{\sqrt{2\rho_{total}}}\right)} \\ &\quad + \rho_{GND}\frac{erf\left(\frac{\rho_{GND}L}{\sqrt{2\rho_{total}}}\right) - \frac{1}{2}erf\left(\frac{q+\rho_{GND}L}{\sqrt{2\rho_{total}}}\right) - \frac{1}{2}erf\left(\frac{q-\rho_{GND}L}{\sqrt{2\rho_{total}}}\right)}{\frac{1}{2}erf\left(\frac{q-\rho_{GND}L}{\sqrt{2\rho_{total}}}\right) + \frac{1}{2}erf\left(\frac{q+\rho_{GND}L}{\sqrt{2\rho_{total}}}\right)} \end{aligned} \quad (5.6)$$

where q is the maximum amount of detectable lattice distortion between patterns divided by Burgers vector. The resulting equation is obviously quite unwieldy and has computational overflow issues at large step sizes (precisely where it differentiates from Eq 5.5) because of exponentials in the numerator of the first term would become too large for double precision variables before being divided. Making the following substitution will allow use to simplify this equation:

$$erf(z) = 1 - exp(-z^2)erfcx(z) \quad (5.7)$$

where $erfcx(z)$ is the scaled complimentary error function. Making this substitution and by assuming that L is large, Equation 5.6 may be simplified to Eq. 5.8, which is stable at high step sizes:

$$\begin{aligned}\bar{\rho}_m &= \frac{\int_{-qL}^{qL} |xf(x,\rho_{total}L^2,\rho_{GND}L^2)|dx}{L^2} \\ &\approx \sqrt{\frac{2}{\pi}}\frac{2exp\left(\frac{q^2-\rho_{GND}^2L^2}{2\rho_{total}}\right) - 1}{erfcx\left(\frac{\rho_{GND}L-q}{\sqrt{2\rho_{total}}}\right)}\frac{\sqrt{\rho_{total}}}{L} + \rho_{GND} \end{aligned} \quad (5.8)$$

This equation is compared to Equation 5.5 in Figure 5.7. Since our simulation had no limit to the number of dislocations, the limit parameter is completely arbitrary to show the potential of the equation. Because it is difficult to deconvolve the various factors that contribute to this limit and because this region of the curve contains little useful dislocation information, we will use q only as a fitting parameter only on real samples.

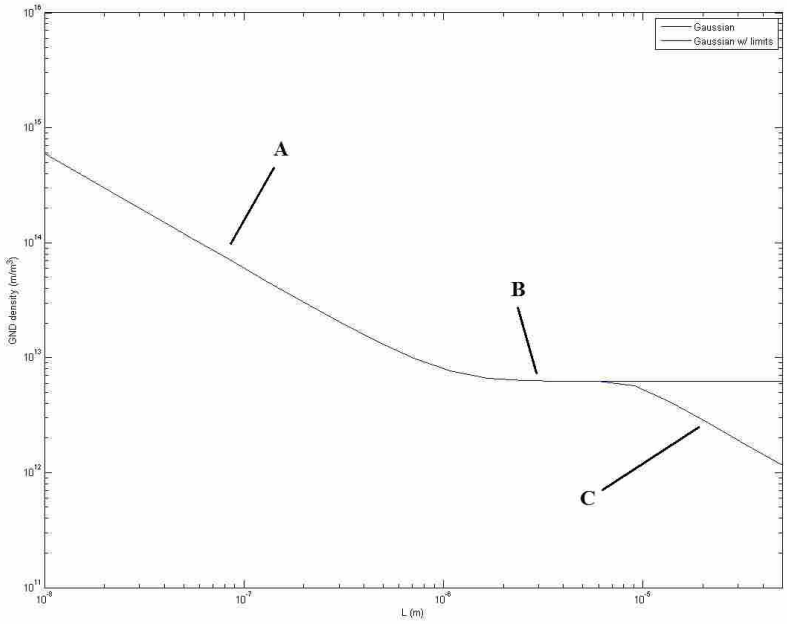

Figure 5.7: The Gaussian model of a GND density versus step size curve is compared with the Gaussian model with limits of integration applied. Note that the two models are indistinguishable until larger step sizes where the model with limits applied drops off, as seen in real data (see Figure 5.2).

This model may be fit to real data using only three parameters, total dislocation density, true GND density, and q. Thus, generating a GND density versus step size curve and fitting this model to it allows us to estimate not only GND density associated with strain gradients, but also the total dislocation density. We fit our Gaussian model to the data for the indented Ta sample discussed in the previous section. The fit was performed by optimizing the three parameters to minimize the sum of the squared error in log space (to fit all regions of the data). The parameters of the curve show that the average total dislocation density over the area of the scan is $5.98 \times 10^{14} m/m^3$ and the density of heterogeneously distributed dislocations (”true” GNDs) is $3.64 \times 10^{14} m/m^3$. The fit is shown in Figure 5.8.

5.4 Conclusions

The variation in EBSD measurements of GND content due to the step size of the numerical derivative of the lattice distortion has been reported multiple times in literature. This relationship is

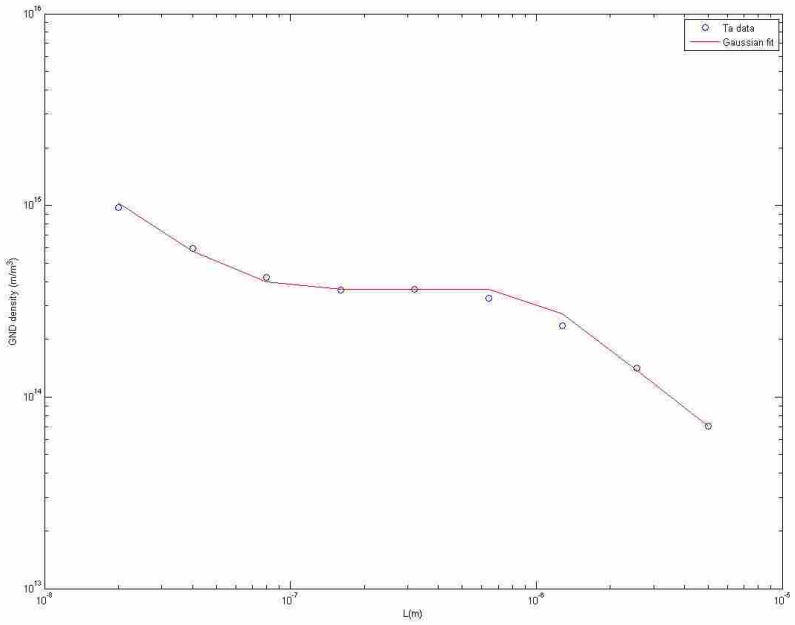

Figure 5.8: The Gaussian model of a GND density versus step size curve with limits is fit to the real data from the indented Ta sample (see Figure 5.2). The parameters used to fit the curve are $\rho_{GND} = 3.64 \times 10^{14} m/m^3$, $\rho_{total} = 5.98 \times 10^{14} m/m^3$, and $q = 3.53 \times 10^8 m^{-1}$

quite complex, and a number of phenomena have been suggested, including noise in the calculation of the lattice distortion due to the resolution limit of the phosphor screen and periodic dislocation structure of a given length scale. This study has found that most variation of the measured GND density may be statistically modeled as the shift of SSDs to GNDs for a randomly distributed field of dislocations.

This model fits a variety of real scans. We validated the model by fitting it to the measured GND density versus step size curve of an indented Ta sample, which suggested that the area scanned had a total dislocation density of $5.98 \times 10^{14} m/m^3$ and a "true" GND density of $3.64 \times 10^{14} m/m^3$. The fit of this curve suggested a significantly higher ratio of "true" GNDs associated with heterogeneous deformation than homogeneously distributed dislocations associated with macro-deformation. Most available data in the literature concerns specimens deformaed in simple tension, where the deformation is more homogeneous. These samples do not typically have a strong B region. These results supports our claim that the B region of GND density curves is associated with "true" geometrically necessary dislocations.

The success of the model allows us to propose robust criteria for step size selection in EBSD dislocation microscopy studies. Once a GND density versus step size curve is generated as explained in this paper by skipping points, the constant region may be identified. This constant region represents a range of potential step sizes that allow the accurate recovery of the GND density at the length scale of the grain.

Perhaps more significantly, the statistical model of GND to SSD transition allows the recovery of the total bulk dislocation density of a material once the model is fit to a measured GND-step size curve. Because all dislocations contribute to the plastic behavior of materials, this represents a significant advance in EBSD dislocation microscopy technology.

CHAPTER 6. CONTRIBUTIONS AND DISCUSSION

EBSD dislocation microscopy allows the recovery of dislocation density information at length scales most relevant to crystal plasticity modeling. The potential it has to improve plasticity modeling is unprecedented. Some workers have already begun directly linking crystal plasticity finite element models to dislocation information collected via EBSD [18], but this is still the exception and not the norm. The slow adoption of EBSD CDM is primarily due to the uncertainties that still plague the technique. True validation of EBSD CDM is severely lacking, and difficulty in solving the basic equations leads to a significant degree of ambiguity in conventional EBSD CDM approaches. Results also tend to fluctuate wildly depending on the length scale dislocation information is observed at. This work has addressed all of these issues, providing robust, accurate and validated ways of determining total dislocation content for any crystalline material, as well as complete dislocation system information for FCC and HCP materials. The ambiguity of length scale was also addressed, showing that the affect of length scale of EBSD CDM measurements actually contains useful information about the total quantity and nature of the dislocation density.

In Chapter 2, a novel method of simulating the distortion fields of continuum networks of dislocations was presented. This simulation is based on adapting classical dislocation mechanics for a continuum view. It has the same accuracy as conventional Greens function techniques [40–42], but is much more computationally efficient. This simulation is used to validate an estimate of the dislocation density based on the entry-wise one-norm of the Nye tensor [13]. We found that by estimating the one-norm of the Nye tensor using all available lattice distortion derivatives, 2D estimates of bulk dislocation density have 20% less noise. This represents an significant improvement over current techniques.

Next, in Chapter 3, we collaborated with another research group to validated EBSD CDM with a sample that underwent a carefully controlled deformation. A nickel single crystal was micro-indented to simulate plastic behavior around a crack tip. FEA [46, 47] and crack mechanics

[48, 49] were used to predict the active dislocations around the indenter tip. A highly constrained version of EBSD CDM was then used to show that these dislocation were in fact present [29, 36]. Using the simulations presented in Chapter 2, existing 2D CDM methods were improved. Our improved Nye-Kroner technique managed to detect the predicted active slip types without having to incorporate any prior assumptions, meaning that Kysar's method of identifying active slip systems may be generalized for any in-plane deformation.

Although these efforts led to a significant improvement on the conventional Nye-Kroner approach to EBSD CDM, Nye-Kroner methods of slip system determination are inherently underconstrained, meaning there is a quite a bit of ambiguity in results. 2D EBSD exacerbates this problem further, making only 1/3 of the terms of the Nye tensor available to constrain the optimization problem required for EBSD CDM (Equation 1.11). We solve this problem in Chapter 4 by directly relating the measured lattice distortion gradients to the dislocation content of the material via the simulated dislocation distortion fields shown in Chapter 2. This quadruples the number of constraints available, and in simulations, this new lattice distortion matching method was found to be a dramatic improvement over conventional Nye-Kroner CDM, effectively identifying the type and quantity of dislocation systems present in simulations regardless of the dislocations orientation relative to the sample surface or the complexity of the dislocation structure. Although this method has not been successfully implemented on real data, it shows potential to supplant existing methods because of its improved accuracy.

Finally, in Chapter 5, the issue of step size was addressed. Measured values of GND density are highly sensitive to the distance between points on the raster of an EBSD scan (which corresponds to the step size of the numerical derivative used to calculate the lattice distortion derivatives). In this chapter, used the concept of GND to SSD transition to statistically model the variation in measured GND density over different step sizes. This model allows us to use GND density versus step size curves to estimate the total dislocation contetn of the material, as well as determine the range of step sizes over which the "true" GND density of the material (the dislocation density associated with strain gradients on the length scale of the substructure) may be determined.

CDM's potential for materials characterization is hampered by limitations of current implementations. The new methods presented in this dissertation may be implemented broadly and

robustly, without making assumptions about the deformation of the material examined. Step size analysis provides new information previously unrecoverable via EBSD CDM. It is the hope of the author, that EBSD CDM will see widespread application as a characterization technique.

REFERENCES

[1] P. Hirsch, A. Howie, and M. Whelan, "A kinematical theory of diffraction contrast of electron transmission microscope images of dislocations and other defects," *Philosophical transactions of the Royal Society of London., A Mathematical and physical sciences*, vol. 252, 1960. 1

[2] B. Fultz and J. Howe, *Transmission Electron Microcopy and Diffraction of Materials*. New York: Springer, 2008. 1

[3] M. F. Ashby, "The deformation of plastically non-homogeneous materials," *Phil. Mag.*, vol. 21, pp. 399–424, 1970. 2, 53

[4] J. Nye, "Some geometrical relations in dislocated crystals," *Acta Metallurgica*, vol. 1, pp. 153–162, 1953. 2, 5

[5] E. Kröner, "Continuum theory of dislocations and self-stresses," *Ergebnisse der Angewandten Mathematik*, vol. 5, pp. 1327–1347, 1958. 2, 5

[6] R. Tissot, "Microdiffraction applications utilizing a two-dimensional proportional detector," *Power Diffraction*, vol. 18, pp. 86–90, 2003. 2

[7] S. I. Wright, "Review of automated orientation imaging microscopy (OIM)," *Journal of Computer-Assisted Microscopy*, vol. 5, no. 3, pp. 207–221, 1993. 2, 5, 6

[8] S. Wright and B. Adams, "Automated lattice orientation determination from electron backscatter Kikuchi diffraction patterns," *Textures and Microstructures*, vol. 14-18, pp. 273–278, 1991. 2, 5

[9] S. I. Wright, B. L. Adams, and K. Kunze, "Application of a new automatic lattice orientation measurement technique to polycrystalline aluminum," *Materials Science and Engineering A*, vol. 160, no. 2, pp. 229–240, 1993. 2, 5

[10] K. Troost, P. van der Sluis, and D. Gravesteijn, "Microscale elastic-strain determination by backscatter kikuchi diffraction in the scanning electron microscope," *Appl. Phys. Lett.*, vol. 62, no. 10, pp. 1110–1112, 1993. 2

[11] A. J. Wilkinson, G. Meaden, and D. J. Dingley, "High resolution mapping of strains and rotations using electron back scatter diffraction," *Materials Science and Technology*, vol. 22, no. 11, pp. 1–11, 2006. 2, 8

[12] ——, "High-resolution elastic strain measurement from electron backscatter diffraction patterns: New levels of sensitivity," *Ultramicroscopy*, vol. 106, pp. 307–313, 2006. 2, 8, 37, 58

[13] B. El-Dasher, B. Adams, and A. Rollett, "Viewpoint: Experimental recovery of geometrically necessary dislocation density in polycrystals," *Scripta Materialia*, vol. 48, no. 2, pp. 141–145, 2003. 3, 9, 10, 13, 69

[14] C. J. Gardner, B. L. Adams, J. Basinger, and D. T. Fullwood, "EBSD-based continuum dislocation microscopy," *International Journal of Plasticity*, vol. 26, pp. 1234–1247, 2010. 3, 7, 27

[15] T. J. Ruggles and D. T. Fullwood, "Estimations of bulk geometrically necessary dislocation density using high resolution EBSD," *Ultramicroscopy*, vol. 133, pp. 8–15, 2013. 3, 10, 56, 57

[16] S. Sun, B. Adams, and W. King, "Observations of lattice curvature near the interface of a deformed aluminium bicrystal," *Philosophical Magazine A: Physics of Condensed Matter, Structure, Defects and Mechanical Properties*, vol. 80, no. 1, pp. 9–25, 2000. 3, 6, 9, 13

[17] A. Wilkinson, E. Clarke, T. Britton, P. Littlewood, and P. Karamched, "High-resolution electron backscatter diffraction: an emerging tool for studying local deformation," *The Journal of Strain Analysis for Engineering Design*, vol. 45, pp. 365–376, 2010. 3

[18] H. Lim, S. Subedi, D. Fullwood, B. Adams, and R. Wagoner, "A practical meso-scale polycrystal model to predict dislocation densities and the Hall-Petch effect," *Materials Transaction*, vol. 55, no. 1, pp. 35–38, 2014. 3, 69

[19] P. Lynch, D. Tomus, C. Bettles, M. Gibson, and A. Stevenson, "A comparative EBSD and micro-XRD study of the intergranular grain structure in CP-Ti," *Nuclear Instruments and Methods in Physics Research A*, vol. 619, pp. 298–301, 2010. 3

[20] A. Schwartz, M. Kumar, B. Adams, and D. Field, *Electron backscatter diffraction in materials science 2nd Ed.*, 2nd ed. New York: Springer, 2009. 3, 14

[21] R. Barabash and G. Ice, *Strain and Dislocation Gradients From Diffraction: Spatially-Resolved Local Structure and Defects*. Singapore: World Scientific Publishing Co. Pte. Ltd., 2014. 6, 8

[22] M. N. Alam, M. Blackman, and D. W. Pashley, "High-angle kikuchi patterns," *Proceedings of the Royal Society A*, vol. 221, pp. 224–242, 1954. 5

[23] J. Kacher, C. Landon, B. L. Adams, and D. Fullwood, "Braggs law diffraction simulations for electron backscatter diffraction analysis," *Ultramicroscopy*, vol. 109, no. 9, pp. 1148–1156, 2009. 7, 8, 58

[24] T. Britton, C. Maurice, R. Fortunier, J. Driver, A. Day, G. Meaden, D. Dingley, K. Mingard, and A. Wilkinson, "Factors affecting the accuracy of high resolution electron backscatter diffraction when using simulated patterns," *Ultramicroscopy*, vol. 110, pp. 1443–1453, 2010. 8

[25] Winkelmann, "Simulation of electron backscatter diffraction patterns," *Microscopy and Microanalysis*, vol. 13, pp. 930–931, 2007. 8

[26] J. Basinger, D. Fullwood, J. Kacher, and B. Adams, "Pattern center determination in EBSD microscopy," *Microscopy and Microanalysis*, vol. 17, pp. 330–340, 2011. 8

[27] C. Maurice, D. Krzysztof, and R. Fortunier, "A method for accurate localisation of EBSD pattern centres," *Ultramicroscopy*, vol. 111, pp. 140–148, 2011. 8

[28] J. Wheeler, E. Mariani, S. Piavzolo, D. Prior, P. Trimby, and M. Drury, "The weighted Burgers vector: a new quantity for constraining dislocation densities and types using electron backscatter diffraction on 2D sections through crystalline materials," *Journal of Microscopy*, vol. 233, pp. 482–494, 2009. 9, 15

[29] J. Kysar, Y. Saito, M. Oztop, D. Lee, and W. Huh, "Experimental lower bounds on geometrically necessary dislocation density," *International Journal of Plasticity*, vol. 26, pp. 1097–1123, 2010. 9, 13, 31, 33, 36, 37, 46, 53, 70

[30] J. Koike, T. Kobayashi, T. Mukai, H. Watanabe, M. Suzuki, K. Maruyama, and K. Higashi, "The activity of non-basal slip systems and dynamic recovery at room temperature in fine-grained AZ31b magnesium alloys," *Acta Mater*, vol. 51, pp. 2055–65, 2003. 9, 24

[31] A. Wilkinson and D. Randman, "Determination of elastic strain fields and geometrically necessary dislocation distributions near nanoindents using electron back scatter diffraction," *Philosophical Magazine*, vol. 90, no. 9, pp. 1159–1177, 2010. 10

[32] M. Calcagnotto, D. Ponge, E. Demir, and D. Raabe, "Orientation gradients and geometrically necessary dislocations in ultrfine grained dual phase steels studied by 2D amd 3D EBSD," *Materials Science and Engineering A*, no. 527, pp. 2738–2746, 2010. 10, 14

[33] L. Kubin and A. Mortenson, "Geometrically necessary dislocations and strain-gradient plasticity: a few critical issues," *Scripta Materialia*, no. 48, pp. 119–125, 2003. 10

[34] E. Demir, D. Raabe, N. Zaafarani, and S. Zaefferer, "Investigation of the indentation size effect through the measurement of the geometrically necessary dislocations beneath small indents of different depths using EBSD tomography," *Acta Materialia*, vol. 57, pp. 559–569, 2009. 13, 14

[35] D. Field, P. Trivedi, S. Wright, and M. Kumar, "Analysis of local orientation gradients in deformed single crystals," *Ultramicroscopy*, vol. 103, pp. 33–39, 2005. 13

[36] J. W. Kysar, Y. Gan, T. Morse, X. Chen, and M. Jones, "High strain gradient plasticity associated with wedge indentation into face-centered cubic single crystals: Geometrically necessary dislocation densities," *Journal of the Mechanics and Physics of Solids*, vol. 55, pp. 1554–1573, 2007. 13, 31, 36, 54, 70

[37] P. Littlewood, T. Britton, and A. Wilkinson, "Geometrically necessary dislocation density distribution in Ti-6Al-4V deformed in tension," *Acta Materialia*, vol. 59, pp. 6489–6500, 2011. 15

[38] W. Pantleon, "Resolving the goemetrically necessary dislocation content by conventional electron backscattering diffraction," *Scripta Materialia*, vol. 58, pp. 994–997, 2008. 15, 21, 32, 45, 47, 51

[39] E. Kröner, "Modified green functions in the theory of heterogeneous and/or anisotropic linearly elastic media," in *Micromechanics and Inhomogeneity*, G. Weng and M. Abe, Eds. Berlin: Springer, 1989, pp. 197–211. 16

[40] T. Mura, "Continuous distribution of moving dislocations," *Philosophical Magazine*, vol. 8, pp. 843–857, 1963. 16, 69

[41] ——, *Micromechanics of Defects in Solids*, 1st ed. Dordrecht: Martinus Nijhoff Publishers, 1982. 16, 69

[42] C. Teodosiu, *Elastic Models of Crystal Defects*. Berlin: Springer-Verlag, 1982. 16, 69

[43] M. Lazar, "Dislocations in the field theory of elastoplasticity," *Computational Materials Science*, vol. 28, pp. 419–428, 2003. 16

[44] Maplesoft, "Maple 15," 2011. 17

[45] K. Krieger Lassen, "Automated determination of crystal orientations from electron backscattering patterns," *PhD thesis, The Technical University of Denmark*, 1994. 27

[46] Y. Saito and J. W. Kysar, "Wedge indentation into elastic-plastic single crystals, 1: Asymptotic fields for nearly-flat wedge," *International Journal of Plasticity*, vol. 27, no. 10, pp. 1640–1657, 2010. 31, 36, 69

[47] Y. Saito, M. S. Oztop, and J. W. Kysar, "Wedge indentation into elastic-plastic single crystals. 2: Simulations for face-centered cubic crystals," *International Journal of Plasticity*, no. 28, pp. 70–87, 2012. 31, 36, 69

[48] J. R. Rice, "Tensile crack tip fields in elastic-ideally plastic crystals," *Mechanics of Materials*, vol. 6, pp. 317–335, 1987. 31, 36, 70

[49] W. Crone, T. Shield, A. Creuziger, and B. Henneman, "Orientation dependence of the plastic slip near notches in ductile FCC single crystals," *Journal of the Mechanics and Physics of Solids*, vol. 52, no. 1, 2004. 31, 36, 70

[50] H. Kuhn and A. Tucker, "Nonlinear programming," *Proc. Second Berkeley Symp. on Math. Statist. and Prob.*, pp. 481–492, 1951. 32, 47

[51] J. Kennedy and R. Eberhart, "Particle swarm optimization," *Proceedings of IEEE International Conference on Neural Networks*, vol. IV, pp. 1942–1948, 1995. 32, 47

[52] L. Evers, W. Brekelmans, and M. Geers, "Scale dependent crystal plasticity framework with dislocation density and grain boundary effects," *International Journal of Solids and Structures*, vol. 41, pp. 5209–5230, 2004. 33, 46

[53] G. I. Taylor, "Plastic strain in metals," *Journal of the Institute of Metals*, vol. 62, pp. 307–324, 1938. 44

[54] D. Field, C. Merriman, N. Allain-Bonasso, and F. Wagner, "Quantification of dislocation structure heterogeneity in deformed polycrystals by EBSD," *Model. Simul. Mater. Sc.*, 2012. 53, 57

[55] D. Field, C. Merriman, and J. Smith, "Excess dislocation density measurement dependence on EBSD step size," *Microsc Microanal*, vol. 13, pp. 920–921, 2007. 53

[56] J. Jiang, T. Britton, and A. Wilkinson, "Measurement of geometrically necessary dislocation density with high resolution electron backscatter diffraction: Effects of detector binning and step size," *Ultramicroscopy*, vol. 125, pp. 1–9, 2013. 53, 57, 58, 59

[57] I. Gutierrez-Urrutia and D. Raabe, "Multistage strain hardening through dislocation substructure and twinning in a high strength and ductile weight-reduced Fe-Mn-Al-C steel," *Acta Materialia*, vol. 60, no. 16, pp. 5791–5802, 2012. 54

[58] D. Hughes, N. Hansen, and D. Bammann, "Geometrically necessary boundaries, incidental dislocation boundaries and geometrically necessary dislocations," *Scripta Materialia*, vol. 48, no. 2, pp. 147–153, 2003. 54

[59] F. Ram, S. Zaefferer, and D. Raabe, "The fidelity analysis of the crystal orientations and-misorientations obtained by the classical electron backscatter diffraction technique," *Journal of Applied Crystallography*, In Review. 58

[60] S. Wright and M. Nowell, "High-speed EBSD," *Advanced Materials and Processes*, vol. 166, no. 2, pp. 29–31, 2008. 58

[61] S. Wright, M. Nowell, and J. Basinger, "Precision of EBSD based orientaion measurements," *Microscopy and Microanalysis*, vol. 17, pp. 406–407, 2011. 58

[62] B. Adams and J. Kacher, "EBSD-based microscopy: Resolution of dislocation density," *Computers, Materials and Continua*, vol. 14, no. 3, pp. 185–196, 2009. 60